Composite Structures 314 (2023) 116950

Contents lists available at ScienceDirect

Composite Structures

journal homepage: www.elsevier.com/locate/compstruct

Modeling of adhesively bonded single scarf CFRP joint behavior using energy-based approach

Hetram Sonwani [a], M. Ramji [a], Sai Sidhardh [b,*]

[a] Engineering Optics Lab, Department of Mechanical and Aerospace Engineering, IIT Hyderabad, Kandi, Telangana 502285, India
[b] Department of Mechanical and Aerospace Engineering, IIT Hyderabad, Kandi, Telangana 502285, India

ARTICLE INFO

Keywords:
Adhesively bonded
CFRP
DIC
Finite difference method
Mechanical behavior
Single scarf joint

ABSTRACT

The mechanical behavior of an adhesively bonded single scarf joined Carbon fiber reinforced polymer (CFRP) laminates under tensile loading is studied. An energy-based analytical model is developed to capture the static response of adhesively bonded single scarf joint specimens. This is a high-fidelity and highly accurate alternative to 3D finite element models commonly employed in the literature. The derived governing differential equations (GDEs) are solved using the finite difference scheme. The numerical results for the global response of the adhesively bonded joints provided by the analytical model are compared and successfully validated with the experimental and FE results. For this purpose, the experimental whole-field technique of 2D digital image correlation (DIC) is used to capture the strain and displacement field over the specimen surface. A qualitative agreement of the field distributions is observed since the analytical model is a reduced-order model. Parametric studies are also undertaken to demonstrate the influence of design parameters, such as scarf angle, adhesive thickness, and adhesive modulus. These results provide quick solutions for the design space of adhesively bonded scarf joints. Therefore, a reliable model for the adhesively bonded single scarf joints is established, acting as a cost-effective and time-saving alternative solution.

1. Introduction

Composite structures are ubiquitous in aerospace, mechanical, civil, and marine industries, among several others. This is owed to their excellent mechanical properties such as high strength-to-weight ratio, stiffness, corrosion resistance, thermal resistance, and fatigue resistance [1,2]. These components experience damage during their service life, commonly due to impact (e.g., bird strike) or by an accident during maintenance (e.g., tool drops) [3–5]. Damage in composite structures degrades the mechanical properties and negatively effects their performance. Therefore, it is crucial to devise methodologies to repair these damages and restore their structural integrity. Existing options for repair are, either by replacing or reinforcing the damaged area [6,7]. In the latter approach, the damaged area is reinforced with an additional patch to restore the strength and stiffness of the damaged composite laminates. However, the additional reinforcement adds a penalty to the weight of the parent structure, thereby effecting the dynamic performance of the parent structure [8]. This is unlike the alternative, where the damaged zone is replaced with a healthy composite patch, with no significant modifications to the weight of the parent structure. More clearly, the damaged zone is cut out, and a replacement patch is joined with the parent structure [4]. This can be achieved in several ways, using techniques such as bonded, bolted, and riveted joints. Among these, the bolted and riveted joints attach the replacement patch to the parent structure using mechanical fasteners. In comparison to this, adhesively bonded joints employ an adhesive to join the components. While the former approach is easier to implement as compared to the adhesively bonded joints, they introduce high stress concentrations at the point of joining that leads to the failure of the joints predominantly [1]. Further, among the existing joining techniques, adhesively bonded joints offer several advantages over its alternatives. This includes a uniform stress distribution at the overlap region, joining with dissimilar materials, greater corrosion and fatigue resistance [9–18].

An adhesive joint connects the adherends (parent structure) via an adhesive layer. There are numerous possible configurations of adhesively bonded joints. Common examples include a simple-lap, butt, scarf, and stepped joint configurations [19]. These configurations differ in the manner the adherends are connected by the adhesive. More clearly, these configurations differ in the manner an overlap region is defined for the adherends and connected by the adhesive layer. It must be noted that these configurations allow the mechanical load to be transferred across the joint by different mechanisms. For instance,

* Corresponding author.
E-mail address: sidhardh@mae.iith.ac.in (S. Sidhardh).

https://doi.org/10.1016/j.compstruct.2023.116950
Received 23 November 2022; Received in revised form 6 February 2023; Accepted 16 March 2023
Available online 24 March 2023

higher stress concentration occurs in the stepped-lap joint as compared to the scarf joint [20]. Also, the scarf joint provides a higher surface area for adhesive contact which in turn enhances the strength of the joint [21,22]. This renders the joint interface to be a critical region after the repair of the parent structure, making it prone to failure [23,24]. Clearly, this observation highlights the importance of their design and analysis. Before undertaking a detailed study of the design of adhesively bonded joints, it is required to develop accurate models for predicting the mechanical behavior of adhesively bonded joints as it will provide a quick and reliable solution from the design point of view.

The two methods that have been preferred by researchers for the design of adhesively bonded joints are analytical and finite element (FE) modeling approaches [20,25,26]. Several researchers have investigated the tensile behavior of an adhesively bonded scarf joint specimen subjected to a static tensile loading using FE modeling [21,26–31]. It is observed that the stresses are high at the overlap edges of the joints. The strength prediction and failure behavior of an adhesively bonded scarf joint are also analyzed experimentally and numerically [32,33]. Further, parametric studies are conducted using linear FE analysis to analyze the effect of scarf angles, laminate thickness, adhesive thickness, and stacking sequences over the behavior of adhesively bonded scarf joints. The influence of these parameters on average and peak stresses at the bond line is also studied [29–31,34–37]. The cohesive zone modeling (CZM) is used to analyze the failure behavior of the adhesive interface in the composite joints [32,38,39]. These studies noted fiber failure for adhesively bonded joints with smaller scarf angles ($\theta < 15°$), while cohesive shear failure is observed in the case of larger scarf angles ($\theta > 15°$) [30].

Several experimental studies are conducted over predicting the mechanical behavior of adhesively bonded joints mainly focusing on the estimation of their stiffness and strength [22,32,40]. Linear (approximately) load–displacement response has been observed for smaller scarf angles ($\theta < 8.13°$), and the lap shear strength is nearly constant for larger scarf angles ($\theta > 8.13°$) [22]. Ridha et al. analyzed the failure behavior of the damaged, undamaged, and repaired panels considering different cohesive law to investigate the failure behavior of the composite joints [41]. They observed that the exponential traction–separation law is insensitive to the assumed adhesive strength, while the linear and trapezoidal cohesive models are sensitive to both adhesive strength and toughness in the case of the repaired panel. Later, an improved numerical methodology has been proposed to characterize the failure initiation, interaction, and progression in the bonded scarf joints [42]. Clearly, the mechanical behavior of the adhesive scarf joint depends on the geometric and material properties of the adhesive and the adherends. For instance, Refs. [27,28,43] noted that the strength of the adhesive joint is higher for smaller scarf angles. Further, the stacking sequence also influences the strength of the scarf joint because of the non-uniform stress and strain field along the bond line. A lower joint strength is observed for the stacking sequence of $[0/45/-45/90]_{2s}$ due to the effect of the corner singularities than $[90/45/-45/0]_{2s}$ laminate. These observations facilitated the development of an improved design methodology by adopting the strain-based failure criteria for different scarf angles [34,35].

The tensile failure behavior of the scarf-repaired composite is investigated experimentally and numerically [24]. They noted that the damage initiation occurred at the interface of 0° plies and propagated throughout the scarf area [24]. Further, the effects of the various parameters on the joint behavior, such as surface preparation, adhesive properties, joint configurations, and environmental factors are also studied [11]. It is noted that the surface preparation influences the joint strength because of the surface integrity presence on the adherend and adhesive layer [11]. The damage tolerance behavior of the scarf joint with bond line flaws under various environmental, geometric, and support conditions has been studied [44]. The geometry of the scarf joint introduces a singularity near the overlap edges of the joints and the crack gets initiated due to the sharp edges of the joints [45]. Finally, optimization studies are conducted to design a tapered scarf and stepped-lap joints for composite patch repair application [20]. Further, the multi-functional optimization is carried out mainly to reduce the stress concentration in the adhesive layer [46].

The above literature is mainly focused on experimental and numerical studies of the mechanical behavior of adhesively bonded joints. Similarly, an analytical approach to model the adhesively bonded joints has been explored earlier [47–49]. The analytical approach is preferred for the parametric study and optimal design of the joint [50]. The extended shear-lag model has been proposed to analyze the scarf and stepped-lap joints behavior [51]. This work is later extended considering the adhesive plasticity, effects of adherend stiffness, and thermal-mismatch [47]. Later, the mechanical behavior of adhesively bonded CFRP scarf joint specimens is studied using the mechanics of material approach [48,49]. A modified semi-analytical model has been proposed for the single scarf joined CFRP laminates [52]. It must be pointed out that the analytical models developed previously are based on an equilibrium approach [38,48,49,53]. While powerful, it is not trivial to extend this approach to complex geometries and configurations. So, in order to alleviate this gap, an analytical model is proposed for predicting the mechanical behavior of adhesively bonded scarf joints following an energy-based approach. This approach facilitates in extending the existing analytical models to complex adhesive joint configurations in a straightforward manner. In this work, the governing differential equations of equilibrium are developed in Section 2. The examples of UD $[0]_{16}$ and quasi-isotropic $[+45/-45/0/90]_{2s}$ CFRP adherends are considered. Section 3 will provide details on the numerical model developed here based on the finite difference method (FDM). Section 4 gives details on specimen fabrication and testing. Section 5 covers the finite element modeling aspect. Section 6 pertains to results and discussions.

2. Problem formulations

In this section, the analytical model is developed for the adhesively bonded scarf joined CFRP UD and quasi-isotropic laminates. The analytical approach developed here is a one-dimensional model for predicting the mechanical response of an adhesively bonded scarf joint when subjected to axial loading. The governing differential equations are obtained here using the energy approach for the single scarf joint configuration.

Fig. 1a depicts the schematic for the single scarf joined CFRP quasi-isotropic laminates. Further, Fig. 1b represents the domain of the single scarf joint for analytical modeling. The Cartesian coordinate system is defined such that the origin is at the left end of this domain along the mid-plane, and the z-axis is defined along the thickness as illustrated in Fig. 1a. Here, h, A_{11}, and A_{55} denote the thickness, and stiffness in axial and shear directions, respectively, of the adherend. Further, E_3, G_3, and h_3 are the elastic modulus, shear modulus, and thickness of the adhesive layer. The expression for A_{11} and A_{55} in terms of the adherend properties are described in the next section. The length of the complete structure (adherends + adhesive) is taken as L, and the length of the joint is L_s (also referred to as the bond length). The length along the scarf angle is referred to as the bond line and its projection along the x-axis is simply the bond length. The longitudinal and transverse displacement are denoted by u and w, respectively. Here, the model is considered to be a 1D and the degrees of freedom at each grid point are as depicted in Fig. 1c. In this figure, u_1, and w_1 represent the displacement of the left adherend in the axial and transverse directions, respectively, and u_2 and w_2 represent the displacements of the right adherend.

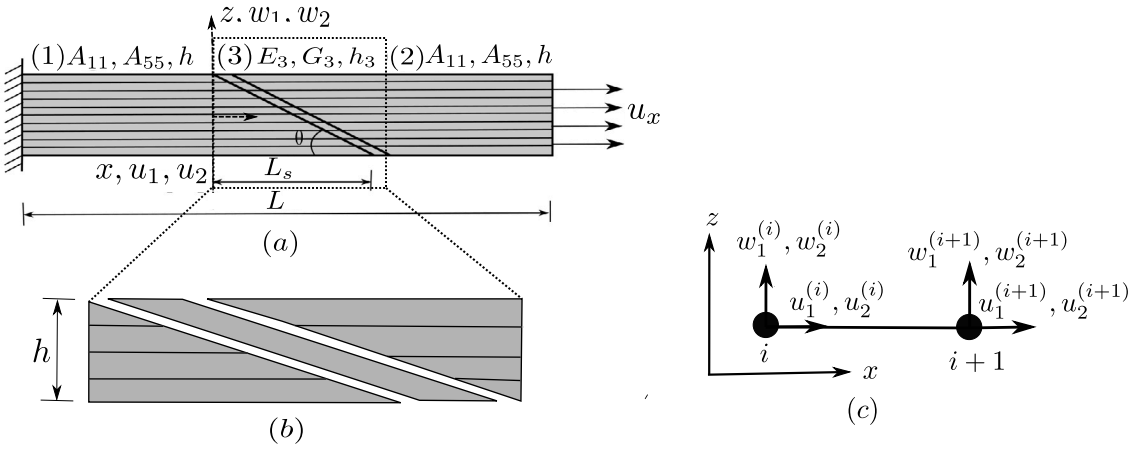

Fig. 1. Adhesively-bonded single scarf joined CFRP quasi-layup: (a) schematic diagram, (b) domain for the analytical modeling, and (c) degree of freedom at grid points.

2.1. Stress–strain relations

The stress–strain relation for the $k-$th lamina in the quasi-isotropic specimen is given in terms of the layup angle (θ_l) as follows [54]:

$$\begin{Bmatrix} \sigma_x^k \\ \sigma_y^k \\ \tau_{xy}^k \end{Bmatrix} = \begin{bmatrix} \overline{Q}_{11}^k & \overline{Q}_{12}^k & \overline{Q}_{16}^k \\ \overline{Q}_{12}^k & \overline{Q}_{22}^k & \overline{Q}_{26}^k \\ \overline{Q}_{16}^k & \overline{Q}_{26}^k & \overline{Q}_{66}^k \end{bmatrix} \begin{Bmatrix} \epsilon_x^k \\ \epsilon_y^k \\ \gamma_{xy}^k \end{Bmatrix} \tag{1}$$

where,

$$\overline{Q}_{11}^k = C_{11}^k = Q_{11}\cos^4\theta_l + 2(Q_{12}+2Q_{66})\sin^2\theta_l\cos^2\theta_l + Q_{22}\sin^4\theta_l$$

$$\overline{Q}_{55}^k = C_{55}^k = Q_{55}\cos^2\theta_l + Q_{44}\sin^2\theta_l$$

Here, $\overline{Q}_{11}^k$ and $\overline{Q}_{55}^k$ are the reduced transformed stiffness matrix in axial and shear directions, respectively. These stiffness matrices are related to the elastic properties in the principal material coordinate system.

The membrane or extensional stiffness in the axial and shear directions for the tapered adherends are expressed as:

$$A_{11} = \sum_{k=1}^{N_l}\int_{h_1^k}^{h_2^k}\overline{Q}_{11}^k\,\mathrm{d}z, \qquad A_{55} = \sum_{k=1}^{N_l}\int_{h_1^k}^{h_2^k}\overline{Q}_{55}^k\,\mathrm{d}z \tag{2}$$

where, A_{11} and A_{55} are the extensional and shear stiffness matrix, respectively. Here, h_1^k and h_2^k are the coordinates of the bottom and top surface for $k-$th lamina along z-axis. N_l is the index of the lamina at the tapered surface. Note that the adhesive joint is a geometrically heterogeneous structure with varying thicknesses along the length. Therefore, the index N_l and thereby the stiffness A_{11} and A_{55} are function of length coordinates.

2.2. Governing equations using energy approach

In this section, the governing equation is derived for the adhesively bonded joint following the principle of minimum potential energy. The statement for minimum potential energy (Π) of the scarf joint (domain is in Fig. 1b) is expressed in terms of the total deformation energy (U) and work done by the external forces (W) as:

$$\delta\Pi = \delta U - \delta W \tag{3}$$

The potential energy is given by:

$$\Pi = \frac{1}{2}\int_v \sigma_{ij}\epsilon_{ij}\,\mathrm{d}v - \int_v f_i u_i\,\mathrm{d}v \tag{4}$$

Here, σ_{ij} and ϵ_{ij} are the stress and strain tensor, respectively. The force and displacement vectors are denoted by f_i and u_i respectively. The subscript v in above equation denotes the domain of the joint. Before proceeding with the derivation of GDEs following the energy approach, the deformation energy of the adherends, adhesive, and the work done by the externally applied forces need to be evaluated. In the subsequent sub-section, the deformation energy of the adherends of a quasi-isotropic layup is formulated. The deformation energy for the UD is a special case of the above-mentioned derivation. Later, the deformation energy for the adhesive layer is also derived. The total deformation energy of the joint will be given by a sum of these energies.

2.2.1. Deformation energy of adherends

The normal and shear stress resultants in the adherends can be expressed as:

$$N_x = A_{11}\frac{\mathrm{d}u}{\mathrm{d}x}, \qquad Q_{xz} = A_{55}\left(\frac{\mathrm{d}w}{\mathrm{d}x} + \frac{\mathrm{d}u}{\mathrm{d}z}\right) \tag{5}$$

In this study, the average stress across the thickness is assumed to be constant and it is uniformly distributed for points away from the taper joint, therefore $\frac{\mathrm{d}u}{\mathrm{d}z} = 0$ over the bond line.

Now, the deformation energy of each of the adherends is evaluated when subjected to axial loading. Note that there are two adherends, and each of these is subjected to axial and transverse shear deformations caused by this axial loading and evaluating each of these energies individually. The variation of the internal energy of the left adherend corresponding to axial deformation is given as:

$$\delta U_{u_1} = \frac{1}{2}\int_0^{L_s} A_{11}^{(1)}\delta\left(\frac{\mathrm{d}u_1}{\mathrm{d}x}\right)^2\mathrm{d}x \tag{6}$$

Also, variation in the axial deformation energy of the right adherend is given as:

$$\delta U_{u_2} = \frac{1}{2}\int_0^{L_s} A_{11}^{(2)}\delta\left(\frac{\mathrm{d}u_2}{\mathrm{d}x}\right)^2\mathrm{d}x \tag{7}$$

Similarly, the variation in the deformation energy corresponding to transverse shear deformation of the left and right adherends is:

$$\delta U_{w_1} = \frac{1}{2}\int_0^{L_s} A_{55}^{(1)}\delta\left(\frac{\mathrm{d}w_1}{\mathrm{d}x}\right)^2\mathrm{d}z, \quad \delta U_{w_2} = \frac{1}{2}\int_0^{L_s} A_{55}^{(2)}\delta\left(\frac{\mathrm{d}w_2}{\mathrm{d}x}\right)^2\mathrm{d}z \tag{8}$$

Using integration by parts for U_{u_1}, we get:

$$\delta U_{u_1} = \frac{1}{2}\int_0^{L_s}\left(A_{11}^{(1)}\frac{\mathrm{d}^2u_1}{\mathrm{d}x^2} + \frac{\mathrm{d}A_{11}^{(1)}}{\mathrm{d}x}\frac{\mathrm{d}u_1}{\mathrm{d}x}\right)\delta u_1\mathrm{d}x - \left(A_{11}^{(1)}\frac{\mathrm{d}u_1}{\mathrm{d}x}\left(\delta u_1(L_s) - \delta u_1(0)\right)\right) \tag{9a}$$

In the above equation, the second expression provides the boundary conditions for the left adherend along the axial direction.

$$\delta U_{w_1} = \frac{1}{2}\int_0^{L_s}\left(A_{11}^{(1)}\frac{\mathrm{d}^2 w_1}{\mathrm{d}x^2} + \frac{\mathrm{d}A_{11}^{(1)}}{\mathrm{d}x}\frac{\mathrm{d}w_1}{\mathrm{d}x}\right)\delta w_1 \mathrm{d}x - \left(A_{11}^{(1)}\frac{\mathrm{d}w_1}{\mathrm{d}x}\left(\delta w_1(L_s) - \delta w_1(0)\right)\right) \tag{9b}$$

In Eq. (9b), the second expression provides the boundary conditions for the left adherend along the transverse direction. Similarly, the deformation energy for the right adherend along the axial and transverse directions can be expressed as:

$$\delta U_{u_2} = \frac{1}{2}\int_0^{L_s}\left(A_{11}^{(2)}\frac{\mathrm{d}^2 u_2}{\mathrm{d}x^2} + \frac{\mathrm{d}A_{11}^{(2)}}{\mathrm{d}x}\frac{\mathrm{d}u_2}{\mathrm{d}x}\right)\delta u_2 \mathrm{d}x - \left(A_{11}^{(2)}\frac{\mathrm{d}u_2}{\mathrm{d}x}\left(\delta u_2(L_s) - \delta u_2(0)\right)\right) \tag{9c}$$

$$\delta U_{w_2} = \frac{1}{2}\int_0^{L_s}\left(A_{11}^{(2)}\frac{\mathrm{d}^2 w_2}{\mathrm{d}x^2} + \frac{\mathrm{d}A_{11}^{(2)}}{\mathrm{d}x}\frac{\mathrm{d}w_2}{\mathrm{d}x}\right)\delta w_2 \mathrm{d}x - \left(A_{11}^{(2)}\frac{\mathrm{d}w_2}{\mathrm{d}x}\left(\delta w_2(L_s) - \delta w_2(0)\right)\right) \tag{9d}$$

The cross-section area of the left adherend at a point x is denoted as $\mathcal{A}_1$ and that of the right adherend is $\mathcal{A}_2$. These areas are functions of x (see Fig. 1b), and can be expressed as:

$$\mathcal{A}_1 = (h - x\tan\theta)b, \quad \mathcal{A}_2 = (x\tan\theta)b \tag{10}$$

Following the definitions given in Eq. (2) and the above results, the extensional stiffness for the left and right adherends are given as follows:

$$A_{11}^{(1)} = \left(\sum_{i=1}^{N_l} C_{11}^i \mathcal{A}_1^i\right), \quad A_{11}^{(2)} = \left(\sum_{i=N_t}^{N_l} C_{11}^i \mathcal{A}_2^i\right) \tag{11a}$$

where C_{11}^i is the elastic modulus of the $i-$th lamina in axial direction. $\mathcal{A}_1^i$ and $\mathcal{A}_2^i$ are the cross-section area of the $i-$th lamina for the left and right adherends, respectively. Here, $i = 1$ is the lamina at the bottom surface ($z = -h/2$) and $i = N_t$ is the lamina at the top surface ($z = h/2$). Note that the lamina at the tapered surface (of the left and right adherends) is denoted by N_l. Clearly, N_l is a variable along the length of the lamina, and it is equal to 1 at the top surface of tapered lamina. For instance, for the left adherend, $N_l = N_t$ at $x = 0$, and $N_l = 1$ for points close to $x = L_s$. Similarly, for the right adherends, $N_l = 1$ at points close to $x = 0$, and $N_l = N_t$ for $x = L_s$. The expressions for the shear stiffness can also be derived in a similar manner as follows:

$$A_{55}^{(1)} = \left(\sum_{i=1}^{N_l} C_{55}^i \mathcal{A}_1^i\right), \quad A_{55}^{(2)} = \left(\sum_{i=N_t}^{N_l} C_{55}^i \mathcal{A}_2^i\right) \tag{11b}$$

The following expressions are derived that are present in Eq. (9a):

$$\frac{\mathrm{d}A_{11}^{(1)}}{\mathrm{d}x} = C_{11}^{N_l} b(-\tan\theta), \quad \frac{\mathrm{d}A_{11}^{(2)}}{\mathrm{d}x} = C_{11}^{N_l} b(\tan\theta), \quad \frac{\mathrm{d}A_{55}^{(1)}}{\mathrm{d}x} = C_{55}^{N_l} b(-\tan\theta), \quad \frac{\mathrm{d}A_{55}^{(2)}}{\mathrm{d}x} = C_{55}^{N_l} b(\tan\theta) \tag{12a}$$

Substituting the above expressions in Eq. (9a), the deformation energy can be simplified as follows:

$$\delta U_{u1} = \frac{b}{2}\int_0^{L_s}\left(A_{11}^{(1)}\frac{\mathrm{d}^2 u_1}{\mathrm{d}x^2} - C_{11}^{N_l}\tan\theta\frac{\mathrm{d}u_1}{\mathrm{d}x}\right)\delta u_1 \ \mathrm{d}x - \left(A_{11}^{(1)}\frac{\mathrm{d}u_1}{\mathrm{d}x}\left(\delta u_1(L_s) - \delta u_1(0)\right)\right) \tag{13a}$$

Repeating the above steps for the remaining terms in the deformation energy for the left and right adherend along the axial and transverse directions, the following results are obtained:

$$\delta U_{w1} = \frac{b}{2}\int_0^{L_s}\left(A_{55}^{(1)}\frac{\mathrm{d}^2 w_1}{\mathrm{d}x^2} - C_{55}^{N_l}\tan\theta\frac{\mathrm{d}w_1}{\mathrm{d}x}\right)\delta w_1 \ \mathrm{d}x$$

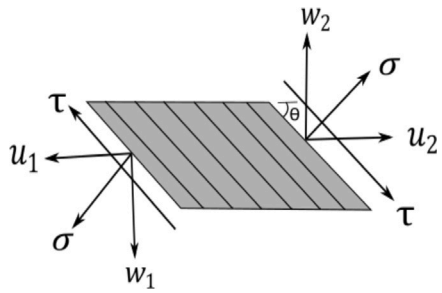

Fig. 2. Free body diagram of an Adhesive layer.

$$- \left(A_{11}^{(1)}\frac{\mathrm{d}w_1}{\mathrm{d}x}\left(\delta w_1(L_s) - \delta w_1(0)\right)\right) \tag{13b}$$

$$\delta U_{u2} = \frac{b}{2}\int_0^{L_s}\left(A_{11}^{(2)}\frac{\mathrm{d}^2 u_2}{\mathrm{d}x^2} + C_{11}^{N_l}\tan\theta\frac{\mathrm{d}u_2}{\mathrm{d}x}\right)\delta u_2 \ \mathrm{d}x - \left(A_{11}^{(2)}\frac{\mathrm{d}u_2}{\mathrm{d}x}\left(\delta u_2(L_s) - \delta u_2(0)\right)\right) \tag{13c}$$

$$\delta U_{w2} = \frac{b}{2}\int_0^{L_s}\left(A_{55}^{(2)}\frac{\mathrm{d}^2 w_2}{\mathrm{d}x^2} + C_{55}^{N_l}\tan\theta\frac{\mathrm{d}w_2}{\mathrm{d}x}\right)\delta w_2 \ \mathrm{d}x - \left(A_{11}^{(2)}\frac{\mathrm{d}w_2}{\mathrm{d}x}\left(\delta w_2(L_s) - \delta w_2(0)\right)\right) \tag{13d}$$

Note that in the above expressions, $A_{11}^{(1)}$, $A_{11}^{(2)}$, $A_{55}^{(1)}$, and $A_{55}^{(2)}$ are variables along x, as seen from Eq. (11). The variation of the total deformation energy of the adherend is:

$$\delta U_{adherend} = \delta U_{u_1} + \delta U_{w_1} + \delta U_{u_2} + \delta U_{w_2} \tag{14}$$

Further, the above expression provides the variation of the deformation energy for quasi-isotropic adherends. For the study on the UD adherends, simply consider $N_t = 1$. This ensures only a single lamina is considered here, and therefore also enforces $N_l = 1$ throughout the joint. The expressions for axial and shear stiffness in Eq. (2) remain unchanged. This choice provides the deformation energy for the adhesively bonded UD adherends.

2.2.2. Deformation energy of adhesive

Fig. 2 shows the free body diagram of the adhesive layer which represents the normal and shear stresses developed on it. The expression for the stresses and strains along axial and transverse directions will be obtained from the free-body diagram of the adhesive layer.

The total deformation energy for the adhesive layer ($U_{adhesive}$) is sum of the deformation energy along axial (U_a) and shear (U_s) directions as given below:

$$U_{adhesive} = U_a + U_s \tag{15}$$

In the subsequent discussion, the analytical expression is derived for U_a and U_s. The expression for strain component along axial and shear directions within the adhesive layer are given as:

$$\epsilon_a = \frac{1}{h_3}(\Delta u\sin\theta - \Delta w\cos\theta), \quad \epsilon_s = \frac{1}{h_3}(\Delta u\cos\theta + \Delta w\sin\theta) \tag{16}$$

where, $\Delta u = u_2 - u_1$, and $\Delta w = w_2 - w_1$, here, subscripts 1 and 2 denote the left and right adherends, respectively. The above expressions are obtained from the schematic in Fig. 2 and are also available in Ref. [38]. The expression for the normal and shear stress components can be expressed as:

$$\sigma_a = \frac{E_3}{h_3}(\Delta u\sin\theta - \Delta w\cos\theta), \quad \sigma_s = \frac{G_3}{h_3}(\Delta u\cos\theta + \Delta w\sin\theta) \tag{17}$$

Here, the adhesive layer is considered an isotropic material. The deformation energy of the adhesive due to axial and shear deformations are

given by:

$$U_a = \frac{1}{2}\int_{v_{adh}} \sigma_a \epsilon_a \, \mathrm{d}v, \qquad U_s = \frac{1}{2}\int_{v_{adh}} \sigma_s \epsilon_s \, \mathrm{d}v, \tag{18}$$

In the above expression, the subscript v_{adh} is a domain corresponding to the adhesive layer. Substituting Eqs. (14) and (17) gives the following results:

$$U_a = \frac{1}{2}\int_{v_{adh}} \frac{E_3}{h_3^2}(\Delta u \sin\theta - \Delta w \cos\theta)^2 \, \mathrm{d}v \tag{19}$$

$$U_s = \frac{1}{2}\int_{v_{adh}} \frac{G_3}{h_3^2}(\Delta u \cos\theta + \Delta w \sin\theta)^2 \, \mathrm{d}v \tag{20}$$

Substituting the above results in Eq. (15) and, one gets the following expression for the adhesive as shown in Fig. 2:

$$\begin{aligned} U_{adhesive} = \int_0^{L_s} \Bigg\{ & \frac{b}{2}\left(\frac{E_3}{h_3}\sin\theta\tan\theta + \frac{G_3}{h_3}\cos\theta\right)\Delta u^2 \\ & + \frac{b}{2}\left(\frac{E_3}{h_3}\cos\theta + \frac{G_3}{h_3}\sin\theta\tan\theta\right)\Delta w^2 \\ & + \left(\frac{-E_3}{h_3}\sin\theta + \frac{G_3}{h_3}\sin\theta\right)\Delta u \Delta w \Bigg\} \, \mathrm{d}x \end{aligned} \tag{21}$$

The above expression corresponds to the total deformation energy in the adhesive layer of a single scarf joint specimen configuration.

2.2.3. GDEs for the adhesively bonded single scarf joint

In the above discussion, the deformation energy for the adherends and the adhesive is derived when the joint is subjected to an axial load. The total deformation energy of the single scarf joint is given by:

$$U = U_{adherend} + U_{adhesive} \tag{22}$$

Finally, the work done by an externally applied axial load as shown in the schematic (Fig. 1) is:

$$W = F_{x_1} u_1|_{x=L_s} + F_{x_2} u_2|_{x=L_s} \tag{23}$$

Substituting these results in Eq. (4) gives the total potential energy of the joint. Applying the principle of minimum potential energy ($\delta\Pi = 0$) gives rise to:

$$\delta\Pi = \frac{\mathrm{d}\Pi}{\mathrm{d}u_1}\delta u_1 + \frac{\mathrm{d}\Pi}{\mathrm{d}w_1}\delta w_1 + \frac{\mathrm{d}\Pi}{\mathrm{d}u_2}\delta u_2 + \frac{\mathrm{d}\Pi}{\mathrm{d}w_2}\delta w_2 = 0 \quad \text{(For equilibrium)} \tag{24}$$

Collecting the variation of the individual degree of freedoms (δu_1, δw_1, δu_2, δw_2), one can get the following GDEs for the left and right adherend along axial and transverse directions:

$$\begin{aligned} & A_{11}^{(1)}\frac{\mathrm{d}^2 u_1}{\mathrm{d}x^2} + (-C_{11}^{N_l}\tan\theta)\frac{\mathrm{d}u_1}{\mathrm{d}x} + \left(\frac{E_3}{h_3}\sin\theta\tan\theta + \frac{G_3}{h_3}\cos\theta\right)\Delta u \\ & + \left(-\frac{E_3}{h_3}\sin\theta + \frac{G_3}{h_3}\sin\theta\right)\Delta w = 0 \end{aligned} \tag{25a}$$

$$\begin{aligned} & A_{55}^{(1)}\frac{\mathrm{d}^2 w_1}{\mathrm{d}x^2} + (-C_{55}^{N_l}\tan\theta)\frac{\mathrm{d}w_1}{\mathrm{d}x} + \left(\frac{E_3}{h_3}\sin\theta - \frac{G_3}{h_3}\sin\theta\right)\Delta u \\ & + \left(-\frac{E_3}{h_3}\sin\theta - \frac{G_3}{h_3}\sin\theta\tan\theta\right)\Delta w = 0 \end{aligned} \tag{25b}$$

$$\begin{aligned} & A_{11}^{(2)}\frac{\mathrm{d}^2 u_2}{\mathrm{d}x^2} + (C_{11}^{N_l}\tan\theta)\frac{\mathrm{d}u_2}{\mathrm{d}x} + \left(-\frac{E_3}{h_3}\sin\theta\tan\theta - \frac{G_3}{h_3}\cos\theta\right)\Delta u \\ & + \left(\frac{E_3}{h_3}\sin\theta - \frac{G_3}{h_3}\sin\theta\right)\Delta w = 0 \end{aligned} \tag{25c}$$

$$\begin{aligned} & A_{55}^{(2)}\frac{\mathrm{d}^2 w_2}{\mathrm{d}x^2} + (C_{55}^{N_l}\tan\theta)\frac{\mathrm{d}w_2}{\mathrm{d}x} + \left(-\frac{E_3}{h_3}\sin\theta + \frac{G_3}{h_3}\sin\theta\right)\Delta u \\ & + \left(\frac{E_3}{h_3}\cos\theta + \frac{G_3}{h_3}\sin\theta\tan\theta\right)\Delta w = 0 \end{aligned} \tag{25d}$$

Note that the above equations are coupled linear ordinary differential equations (ODEs) subjected to the following boundary conditions:

$$x = 0 \ : \qquad u_1(0) = 0, \quad w_1(0) = 0, \quad u_2(0) = 0, \quad w_2(0) = 0 \tag{26a}$$

$$x = L_s \ : \quad u_1(L_s) = u_x, \quad w_1(L_s) = 0, \quad u_2(L_s) = u_x, \quad w_2(L_s) = 0 \tag{26b}$$

As mentioned earlier, the GDEs are developed for quasi-isotropic adherends. Following certain choices for a number of laminae and their material properties (as discussed earlier), these GDEs can be reduced for UD adherends. This is a straightforward derivation, hence skipped here for the sake of brevity. Therefore, in this section, the governing differential equations are derived for the adhesively bonded single scarf joint in Eq. (25) along with the boundary conditions given in Eq. (26). Solving this system of equations will present the elastic response of the same.

2.3. Stresses in the adhesive layer

Before proceeding to the discussion on the numerical method employed here, the derivation for stresses in the adhesive layer is provided. These stresses deserve special focus given their importance in the design of adhesive joints. The normal and shear stresses in the adhesive layer are obtained by resolving the displacements along global coordinate axes as illustrated in Fig. 2. More clearly, the relative displacement in x- and z-directions, and their associated strain and stresses along normal and shear directions are evaluated. Finally, the normal and transverse shear stresses in the adhesive layer are estimated using Eq. (17).

3. Numerical method

The governing differential equations in Eq. (25) can be recast as following:

$$a_1\frac{\mathrm{d}^2 u_1}{\mathrm{d}x^2} + b_1\frac{\mathrm{d}u_1}{\mathrm{d}x} + c_1\Delta u + d_1\Delta w = 0 \tag{27a}$$

$$a_2\frac{\mathrm{d}^2 w_1}{\mathrm{d}x^2} + b_2\frac{\mathrm{d}w_1}{\mathrm{d}x} + c_2\Delta u + d_2\Delta w = 0 \tag{27b}$$

$$a_3\frac{\mathrm{d}^2 u_2}{\mathrm{d}x^2} + b_3\frac{\mathrm{d}u_2}{\mathrm{d}x} + c_3\Delta u + d_3\Delta w = 0 \tag{27c}$$

$$a_4\frac{\mathrm{d}^2 w_2}{\mathrm{d}x^2} + b_3\frac{\mathrm{d}w_2}{\mathrm{d}x} + c_4\Delta u + d_4\Delta w = 0 \tag{27d}$$

where,

$$a_1 = A_{11}^{(1)}, \quad b_1 = -C_{11}^{N_l}\tan\theta, \quad c_1 = \left(\frac{E_3}{h_3}\right)\sin\theta\tan\theta + \left(\frac{G_3}{h_3}\right)\cos\theta,$$

$$d_1 = \left(-\frac{E_3}{h_3}\right)\sin\theta + \left(\frac{G_3}{h_3}\right)\sin\theta, \quad a_2 = A_{55}^{(1)}, \quad b_2 = -C_{55}^{N_l}\tan\theta,$$

$$c_2 = \left(\frac{E_3}{h_3}\right)\sin\theta - \left(\frac{G_3}{h_3}\right)\sin\theta, \quad d_2 = \left(-\frac{E_3}{h_3}\right)\cos\theta - \left(\frac{G_3}{h_3}\right)\sin\theta\tan\theta,$$

$$a_3 = A_{11}^{(2)}, \quad b_3 = -b_1, \quad c_3 = -c_1, \quad d_3 = -d_1, \quad a_4 = A_{55}^{(2)},$$

$$b_4 = -b_2, \quad c_4 = -\left(\frac{E_3}{h_3}\right)\sin\theta + \left(\frac{G_3}{h_3}\right)\sin\theta, \quad d_4 = -d_2$$

The governing differential equations derived here for displacement field variables (u_1, u_2, w_1, and w_2) are solved using the finite difference method (FDM). FDM is simpler, solves the strong form, and is less computationally less expensive to solve equations via the finite difference method. By this method, the ODEs in Eq. (27) are converted to a system of algebraic equations and then boundary conditions are applied as given in Eq. (26) are employed. In this work, 300 uniformly distributed grid points are taken along the bond length of the joint. This choice has been verified based on convergence studies as demonstrated

Table 1
Dimensions of the single scarf joined CFRP UD and quasi-isotropic laminates.

Parameters	Quasi-Layup	UD-Layup
Length of the specimen, L (mm)	210	210
Width of the specimen, b (mm)	20	20
Thickness of the specimen, h (mm)	4.3	4.6
Bond length of adhesive layer L_s (mm)	41.00	43.77
Thickness of the adhesive layer, h_3 (mm)	0.46	0.48
Scarf angle, θ (degree)	6	6

Table 2
Material properties for the adherends and adhesive layer [38].

Material Properties	Values
Adherends:	
Longitudinal modulus, E_{11} (GPa)	105.68
Transverse modulus, $E_{22} = E_{33}$ (GPa)	4.64
In Plane Poisson's ratio, $\nu_{12} = \nu_{13}$ (–)	0.36
Out of Plane Poisson's ratio, ν_{23} (–)	0.49
In Plane Shear modulus, $G_{12} = G_{13}$ (GPa)	3.34
Out of Plane Shear modulus, G_{23} (GPa)	1.55
Adhesive Layer:	
Elastic modulus, E_3 (GPa)	1.68
Poisson's ratio, ν_3 (–)	0.4

in Section 6.3. In the present study, the central finite difference scheme is employed at all the mid-grid points, while boundary conditions are applied at the boundary grid points. Applying the finite difference scheme to the governing differential equations which is recasted as:

$$r_{a_1} u_1^{(i+1)} + r_{b_1} u_1^{(i)} + r_{c_1} u_1^{(i-1)} + d_1 w_2^{(i)} - d_1 w_1^{(i)} = 0 \tag{28}$$

where, $r_{a_1} = \left(\frac{a_1}{\Delta x^2} + \frac{b_1}{2\Delta x}\right)$, $r_{b_1} = \left(\frac{-2a_1}{\Delta x^2} - c_1\right)$, $r_{c_1} = \left(\frac{a_1}{\Delta x^2} - \frac{b_1}{2\Delta x}\right)$

The coefficients a_1, b_1, c_1, and d_1 are provided in Eq. (27).

$$r_{a_2} w_1^{(i+1)} + r_{b_2} w_1^{(i)} + r_{c_2} w_1^{(i-1)} + c_2 u_2^{(i)} - c_2 u_1^{(i)} + d_2 w_2^{(i)} = 0 \tag{29}$$

where, $r_{a_2} = \left(\frac{a_2}{\Delta x^2} + \frac{b_2}{2\Delta x}\right)$, $r_{b_2} = \left(\frac{-2a_2}{\Delta x^2} - d_2\right)$, $r_{c_2} = \left(\frac{a_2}{\Delta x^2} - \frac{b_2}{2\Delta x}\right)$

$$r_{a_3} u_2^{(i+1)} + r_{b_3} u_2^{(i)} + r_{c_3} u_2^{(i-1)} - c_3 u_1^{(i)} + d_3 w_2^{(i)} - d_3 w_1^{(i)} = 0 \tag{30}$$

where, $r_{a_3} = \left(\frac{a_3}{\Delta x^2} + \frac{b_3}{2\Delta x}\right)$, $r_{b_3} = \left(\frac{-2a_3}{\Delta x^2} + c_3\right)$, $r_{c_3} = \left(\frac{a_3}{\Delta x^2} - \frac{b_3}{2\Delta x}\right)$

$$r_{a_4} w_2^{(i+1)} + r_{b_4} w_2^{(i)} + r_{c_4} w_2^{(i-1)} + c_4 u_2^{(i)} - c_4 u_1^{(i)} - d_4 w_1^{(i)} = 0 \tag{31}$$

where , $r_{a_4} = \left(\frac{a_4}{\Delta x^2} + \frac{b_4}{2\Delta x}\right)$, $r_{b_4} = \left(\frac{-2a_4}{\Delta x^2} + d_4\right)$, $r_{c_4} = \left(\frac{a_4}{\Delta x^2} - \frac{b_4}{2\Delta x}\right)$.

The set of algebraic equations over all the grid points chosen along the length of the adhesive bond can be expressed in a matrix form:

$$[P]\{X\} = \{Q\} \tag{32}$$

where $[P]$ is the weighting coefficient matrix, $\{X\}$ is the vector of unknown displacement at the grid-points.

4. Experimental work

The mechanical behavior of the composite structure is studied experimentally for the sake of validation of the analytical model developed here. The experimental work consists of the following steps: (i) fabrication of the CFRP laminate, (ii) machining for obtaining the scarf geometry, (iii) adhesive bonding of the adherends, (iv) testing of the single scarf specimen, and (v) post-processing of the acquired images using VIC-2D software. These steps will be discussed in detail in the subsequent subsections. The dimensions of the single scarf joint for experimental studies are given in Table 1.

4.1. Specimen fabrication

The specimen is an adhesively bonded single scarf joint. Two CFRP adherends are bonded using the adhesive Araldite 2015. The single scarf joined CFRP laminates are fabricated for both UD and quasi-layups. A CFRP dry fabric weighing 230 GSM is placed layer-wise to prepare the laminates. The matrix material contains an epoxy resin (CY 230) and hardener (HY 951) taken in a weight ratio of 10:1. The CFRP laminates of 300×240 mm^2 are fabricated using the hand lay-up process under vacuum bagging process which is cured at room temperature for 24 hours as shown in Fig. 3(a). The laminates are then machined in the CNC milling machine to get a tapered scarf geometry of the required dimensions as shown in Fig. 3(b). The two adherends are bonded using adhesive and then cured in vacuum bagging at room temperature for 24 hours. The material properties of the CFRP adherends and the adhesive layer chosen for the experiment are provided in Table 2 which is taken from Ref. [38]. The bond layer surface is roughened before the bonding using an emery paper and later cleaned using acetone. These steps are undertaken to enhance the bond strength of the joints. The rectangular acrylic strips seen in Fig. 4(a) are used to create a mold for holding the CFRP adherend that constrains the movement of the adherends. The mold dimension is the same as that of the specimen. Wax is applied over the cavity which helps in removing the specimen after curing. As seen in Fig. 4(b), aluminum tabs are bonded over the specimen at the free ends for providing a better grip during the loading.

The random speckle pattern generated over the specimen surface using an air brush is depicted in Fig. 4(c). The specimen surface is coated using white flat paint and then the random speckle pattern is generated with the help of an air brush.

4.2. Experimental setup and test procedure

The single scarf joint specimen is tested using a computer-controlled MTS Landmark™ servo-hydraulic machine of 100 kN capacity. The specimens are subjected to tensile loading under displacement control mode and the tests are carried out at the rate of 0.1 mm/min. Hydraulic grips are used to prevent the slippage of the specimen. The load and displacement data are collected from the data acquisition system connected to the universal testing machine. For the strain analysis, 2D digital image correlation (DIC) setup is used to obtain the whole field displacement and strain fields over the specimen surface. In this technique, the random speckle pattern is generated on the surface of the specimen. A charge-coupled device (CCD) camera is used to capture the speckle images upon loading during the experiment. The images are captured over the thickness face of the specimen. The load and displacement values of every image are stored in the system and the commercial software VIC-Snap software is employed for acquiring these images. VIC-2D software is used for post-processing of the acquired images in order to obtain the strain and displacement field data over the specimen surface. Fig. 5 shows the complete experimental setup employed for the tensile testing of the adhesive-bonded single scarf joined CFRP specimens.

5. Finite element model

In this section, a discussion regarding FE modeling is provided to capture the mechanical behavior of the single scarf joined CFRP UD and quasi-isotropic laminates. In this work, the commercial FE package ABAQUS is used. The geometry and the material properties of the adhesive bonded single scarf joined CFRP UD and quasi-isotropic laminates are given in Table 1 and Table 2 respectively. The CFRP adherends are considered as an orthotropic material, while the adhesive layer is isotropic. The interface between the adherend and adhesive layer is assumed to be perfectly bonded to each other. The applied load and boundary conditions of the finite element model are depicted in Fig. 6(a). The displacement is applied over one end of the model whereas it is constrained in all directions at the other end. In the FE model, an eight-noded linear brick element with reduced integration (C3D8R) is used for meshing purposes as depicted in Fig. 6(b). As clear from this figure, a fine mesh is employed at the joint section to capture the sharp variations in strain and stress fields at points close to the bond surface.

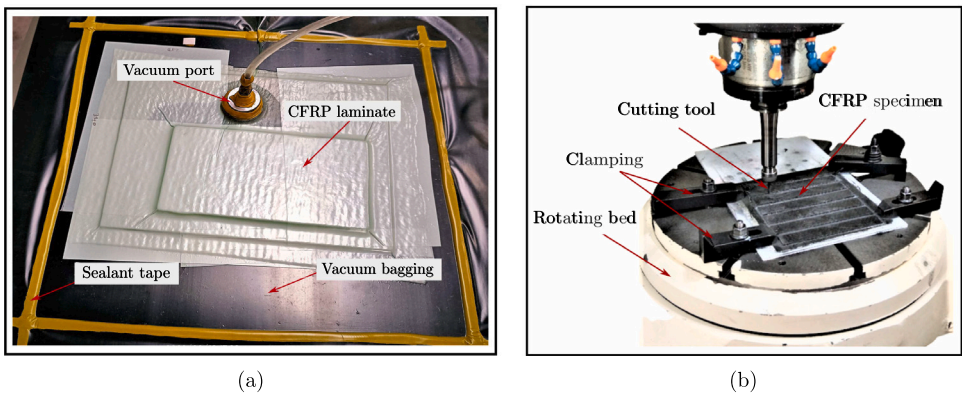

Fig. 3. Specimen fabrication process: (a) vacuum bagging process and (b) machining of the laminate.

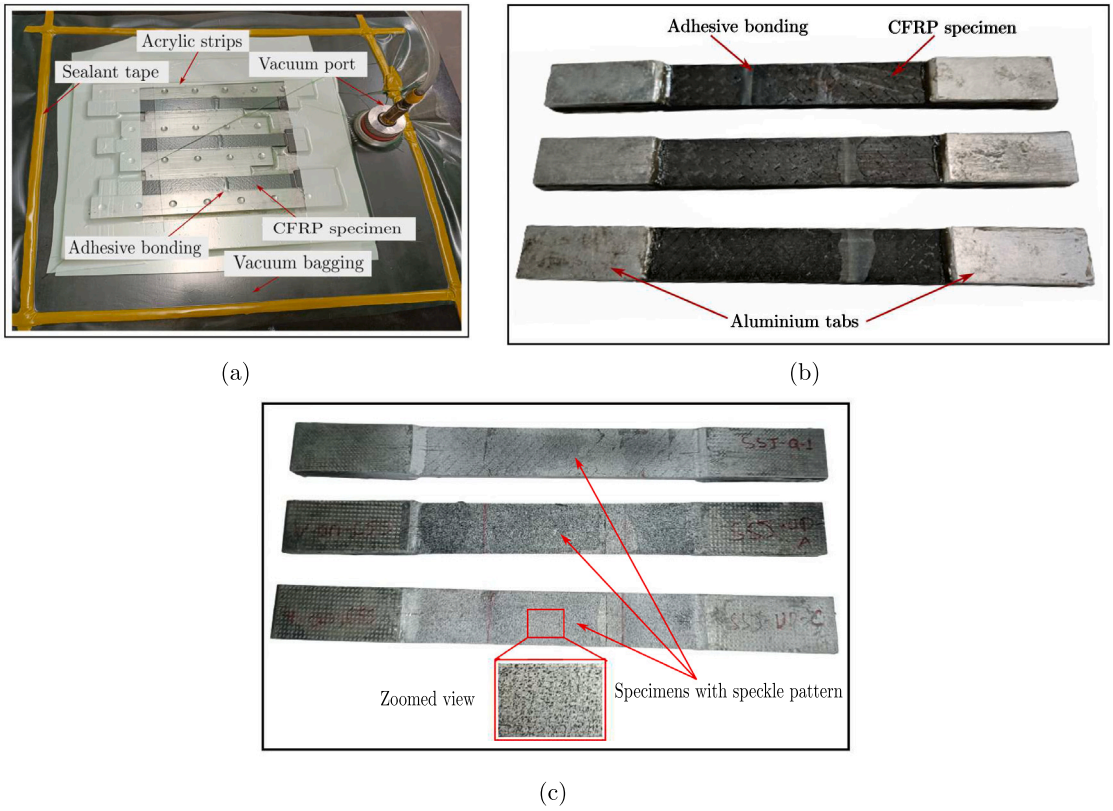

Fig. 4. Bonding of the CFRP adherends: (a) specimens under the vacuum bagging, (b) fabricated adhesive bonded specimens with aluminium tabs, and (c) specimens with speckle pattern.

6. Results and discussions

Before proceeding with a detailed numerical analysis based on the analytical model developed here, the results are presented from experimental and FE analysis. In this section, the experimental and analytical results for the single scarf joined CFRP UD and quasi-isotropic layup sequence is discussed. For the numerical results obtained from the analytical model, a convergence study followed by validation/comparison is discussed. For the experimental results, the structural-level response, like the load–displacement curve, is extracted from the MTS controller. The local field distributions of displacement and strain are deduced from DIC technique.

6.1. Experimental analysis

6.1.1. Single scarf joint UD-layup

The load-deformation curve shown in Fig. 7 is obtained experimentally for the single scarf joint UD specimens. Three specimens are tested and it is observed that the load varies linearly until the peak load and subsequently fails suddenly due to the adhesive disbond. The stiffness in the linear elastic response is nearly the same for all three specimens. From Fig. 7, it is clear that the nonlinear behavior is detected just before the peak load which could be attributed to the accumulated damage. It is noted that the analytical model proposed here only studies the behavior of a single scarf CFRP joint within the

Fig. 5. Experimental setup for the tensile testing of the adhesive bonded scarf joined CFRP specimen.

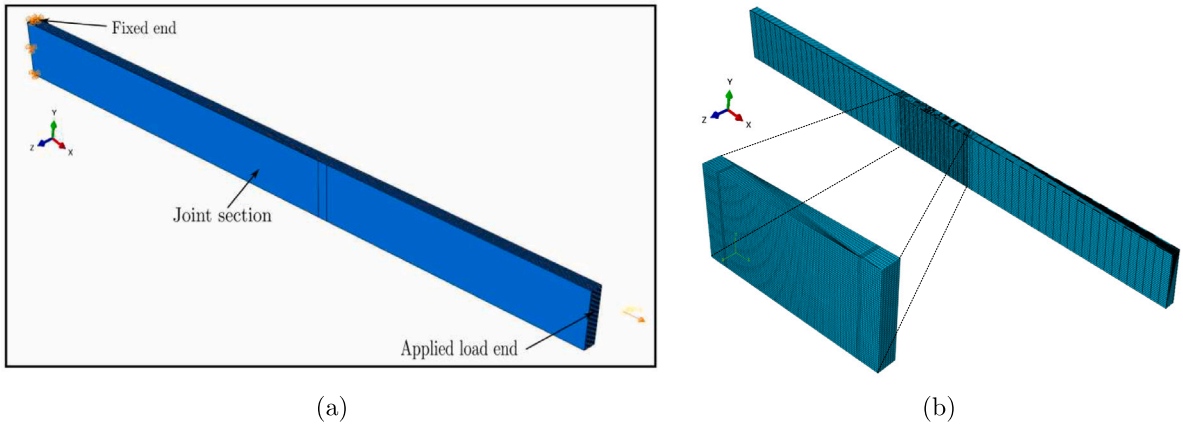

Fig. 6. Single scarf joint configuration of quasi-layup sequence: (a) load and boundary conditions and (b) meshed model.

elastic region. This is because the analytical model does not model damage initiation and propagation within the adhesive joint. However, the analytical model developed here for the linear behavior may be extended to include the plastic effect or progressive damage following appropriate modifications which could be a separate work by itself.

Fig. 8 shows the contour plots of the strain distributions over the thickness face of a single scarf joined UD-layup specimen. These results are obtained from the 2D-DIC technique estimated at a load of 8.3 kN. This load is considered for a better representation of the contour plots without any damage initiation over the specimen. From Fig. 7, it is clear that no damage got initiated in the joint at this load. It is observed that the peak strains occur along the axial directions at the locations 1 and 2 i.e. higher numerical values for strain are noted at the overlap of the joint within the specimen.

Fig. 8(b) depicts the contour plots of the transverse shear strain obtained over the thickness face of the specimen. It is observed that the higher shear strains occur at the locations 3 and 4 similar to the locations 1 and 2 in the axial strain distribution. The distributions of the axial displacement over the thickness face of the specimen in Fig. 8(c) are obtained from 2D DIC. Fig. 8(d) depicts the final failure of the UD-layup specimen. In this figure, the adhesive layer got disbonded at the overlap edge and the damage propagated along the bond line before complete separation. Clearly, the damage gets initiated at the high strain concentration zones at the overlap region, and then propagates through/along the adhesive layer.

6.1.2. *Single scarf joint quasi-isotropic layup*

The above experiments are repeated for the single scarf joint made of the quasi-isotropic adherend and the load-displacement curves are depicted in Fig. 9. The observations seen here are very similar to those seen for UD-layup. Linear elastic behavior is noted until the ultimate load is followed by a sudden drop due to the disbonding of the adhesive layer. It is observed that the slope of the load–displacement curves is the same for all the specimens. Fig. 10 shows the contour plots of the longitudinal strain over the thickness face of the single scarf joint quasi-layup specimen obtained from the DIC experiment taken at a load of 6.43 kN. This value is chosen as the peak load for the linear elastic response of the adhesively bonded single scarf joints. It is

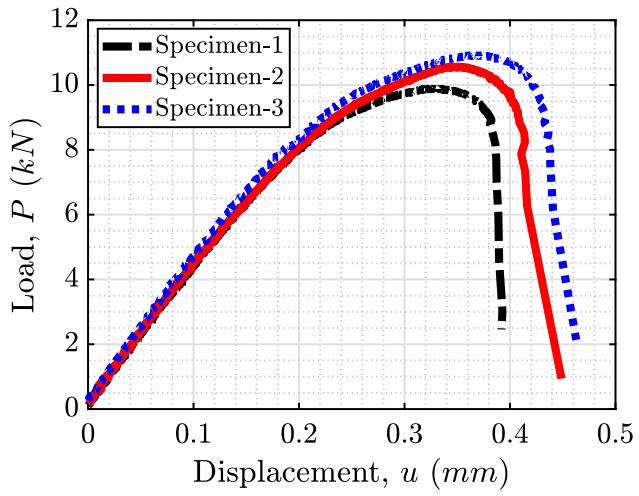

Fig. 7. Experimental load–displacement curve obtained for the single scarf joined CFRP UD-layup sequence $[0]_{16}$.

observed that the peak strains along the axial directions are shown at the locations 5 and 6 as illustrated in Fig. 10(a). This indicates a higher strain concentration at the overlap edge of the specimen. Higher shear strain magnitude is also seen at the locations 7 and 8 (at 0° plies) along the bond line.

Fig. 10(c) shows the failed single scarf joined quasi-layup specimen along the bond line.

6.2. Finite element analysis

In this work, some results are presented for the mechanical behavior of adhesive joints as obtained from the FE study. The contour plot of axial strain (ϵ_{xx}) distribution over the adhesive layer of the single scarf joined UD and the quasi-layup specimen is depicted in Fig. 11. It is observed that the magnitude of axial strain is higher at the overlap edge, while nearly constant over the mid-region in the case of the single scarf joined UD-layup specimen as seen in Fig. 11(a). In contrast to this, the axial strain over the adhesive layer in the case of quasi-isotropic adherends varies along the bond length. This is attributed to the varying stiffness of the lamina bonded to the adhesive layer along the thickness of the quasi-isotropic laminate.

Fig. 12 depicts the contour plots of shear strain (ϵ_{xz}) distributions in the adhesive layer of the single scarf joined UD and quasi-isotropic laminates. The peak strain occurs at the overlap edge of the joint for both UD and quasi-layup specimens. The shear strain is approximately constant at the mid-section of the adhesive bond line in the case of UD-layup specimen but varies in the case of quasi-layup specimen because of different stacking sequences across the thickness as depicted in Fig. 12(b).

6.3. Analytical results

Before employing the finite difference-based model for further studies on the mechanical behavior of adhesive scarf joints, a convergence study is conducted to zero in on the number of grid points. The 1D model is divided into a number of grid points and the displacement along the axial and transverse directions is evaluated at each grid point for the single scarf joined UD and quasi-isotropic layup case.

6.3.1. Convergence study

The load–displacement curves corresponding to different choices for the number of grid points are provided in Fig. 13. This is essential to ensure convergence of numerical results following the finite difference scheme employed here. Note that this study is important in the presence of a very sharp corner at the overlap edges of the joints, as seen in the case of scarf joint configuration. From the figure, it is noted that the load–displacement curves sufficiently converged at 50 grid points for both UD and quasi-layups. Further, the numerical results for 100, 300, and 500 grid points are also provided there to justify the convergence. The convergence of the axial strain distributions along a normalized bond length for the single scarf joined UD and quasi-isotropic laminates are depicted in Fig. 14. The structural level response, like the load–displacement curve, got converged at 50 grid points, while the strain distribution along the bond length is at 300 grid points. Therefore, the 300 grid points are chosen for the subsequent studies based on the finite difference solver for the analytical model.

The shear stress distributions obtained along the normalized coordinates in the adhesive layer of the single scarf joint configuration are plotted for both UD and quasi-layup specimens and it got converged in 300 grid points is depicted in Fig. 15.

6.3.2. Validation

In this section, validation of the proposed analytical model with experimental and FE results is carried out for the single scarf joint configuration. Note that the model developed here is a 1D reduced-order model representing a heterogeneous 3D structure. Therefore, one can compare the structural level response between the 1D and 3D models in order to establish the efficiency of the analytical model. Further, a comparison of the strain and stress distribution across the domain is also carried out. This is to establish a qualitative comparison of the field distributions, but one can expect a quantitative difference between 1D and 3D results. Because the data extracted from DIC and FE shows a minor difference due to different choices for the selection of the exact location of the representative line for the numerical results when compared to the analytical model. Since the analytical model is a 1D line, one has a single choice for the line path. This difference is greater for quasi-isotropic adherends exhibiting greater heterogeneity across the thickness. The load–displacement curves for the single scarf joined CFRP UD and quasi-isotropic laminates are obtained from the analytical model and then compared with the experimental and FE results for each of the cases in Fig. 16. Clearly, the results present an excellent agreement. This validates the analytical model developed here for the adhesively bonded single scarf joint and also the numerical method employed for its solution.

Fig. 17 depicts the shear strain distributions obtained along the normalized coordinates for the single scarf joined UD and quasi-layup configuration obtained from the analytical model and further, the result is compared with DIC and FE predictions. It is observed that the magnitude of shear strain is greater near the overlap edge of the joint while being nearly constant over the mid-section of the normalized coordinates in the case of UD-layup. This is in very good agreement with a similar observation noted previously from FEM in Fig. 12. The shear strain varies along the normalized coordinates due to different stacking sequences in the CFRP quasi-layup specimen. This observation is in also demonstrated by the analytical model and agrees with the results in Ref. [52].

The strain component normal to the adhesive bond line is referred to as the peel strain. A schematic illustration of the line is depicted in Fig. 18(c). The peel strain distribution along the normalized coordinates for the single scarf joined UD and quasi-layup specimens are obtained from the analytical model and then compared with DIC and FE predictions in Fig. 18. There is a good agreement between analytical and FE/experimental predictions.

Fig. 19 depicts the axial strain distribution of the left adherend obtained along the normalized bond length for the single scarf joined CFRP UD and quasi-layups as predicted by the analytical model, and later compared with predictions from DIC, and FE model. It is observed that axial shear strain concentration is greater at the overlap edges and is approximately constant at the mid-section of the bond length

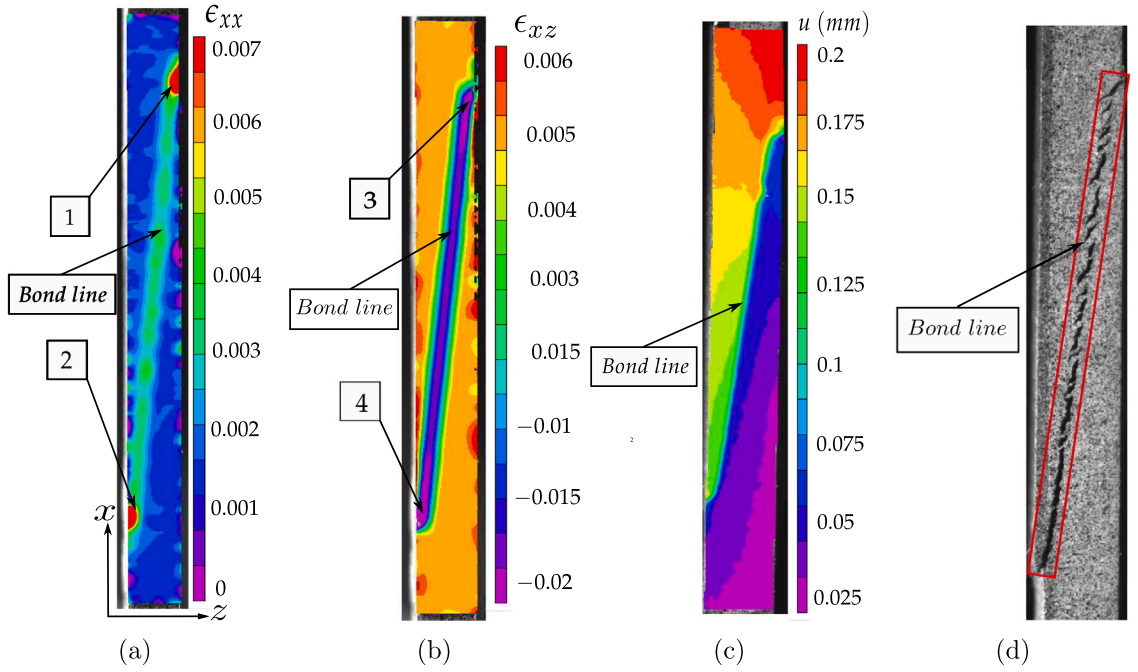

Fig. 8. Strain distributions over the thickness face of the specimen for the single scarf joint UD-layup configuration obtained using 2D DIC technique at 8.3 kN load: (a) axial strain, (b) shear strain, (c) axial displacement distribution, and (d) failure along the bond line.

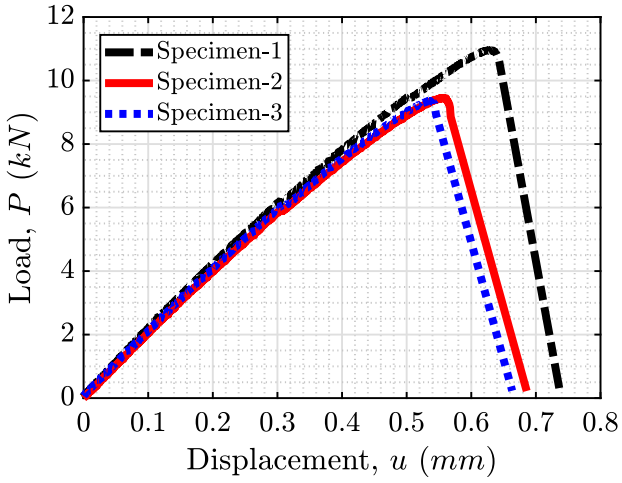

Fig. 9. Experimental load–displacement curve for the single scarf joined CFRP quasi-layup sequence $[45/-45/0/90]_{2s}$.

for UD and varies slowly across the lamina in the case of quasi-layup specimens. This result emphasizes the qualitative agreement between the analytical model prediction with the experimental and numerical studies. As mentioned earlier, this difference is expected since the analytical model is a 1D where one has to consider a single line path. While the results provided above are for a left adherend (LA), a similar observation may be drawn for right adherend (RA), and the results here are not presented for the sake of brevity. The results obtained from the analytical model for the single scarf joined UD-layup are good in agreement with the literature [48].

6.4. Parametric studies

In this section, parametric studies are conducted to deduce the influence of different geometric and material properties of the adhesively bonded joint over its mechanical behavior. The results are taken from the proposed analytical model.

6.4.1. Effect of scarf angle

The load–displacement curves predicted for different scarf angles both for the single scarf joined UD and quasi-layups are depicted in Fig. 20. It is observed that the stiffness of the adhesively bonded single scarf joint increases with increasing scarf angles. These results are in good agreement with the literature [21,22]. The stiffness is greater for larger scarf angles in both single scarf-joined UD and quasi-isotropic laminates. In the plot, the healthy structure is defined as a solid laminate without joints.

The normal stress distribution obtained along the normalized bond length for the left adherend of the single scarf joined UD and quasi-layup specimens predicted for different scarf angles are shown in Fig. 21. It is observed that the normal stress increases with scarf angle for both UD and quasi-isotropic laminates. This implies that a higher stress concentration at the overlap edges develops with increasing scarf angles, making it susceptible to adhesive layer disbond initiation at these regions.

Fig. 22 depicts the shear stress distribution obtained along the normalized coordinates over the adhesive in the case of the single scarf joined UD and quasi-layups having different scarf angles. The shear stress near the overlap edges of the joint is greater for a larger scarf angle. The predictions are in good agreement with the literature [20]. The adhesive disbond may initiate firstly at the overlap edges for a larger scarf angle configuration.

The peel stress distribution obtained along the normalized coordinates over the adhesive layer for adhesively bonded single scarf joints for different scarf angles is depicted in Fig. 23. It is observed that the peel stress increases with scarf angle making them more susceptible to failure. This is in good agreement with the literature [20,29,29,31]. The increasing shear stress magnitude for larger scarf angles could be one of the reasons for cohesive shear failure as observed in the experimental study [32,38].

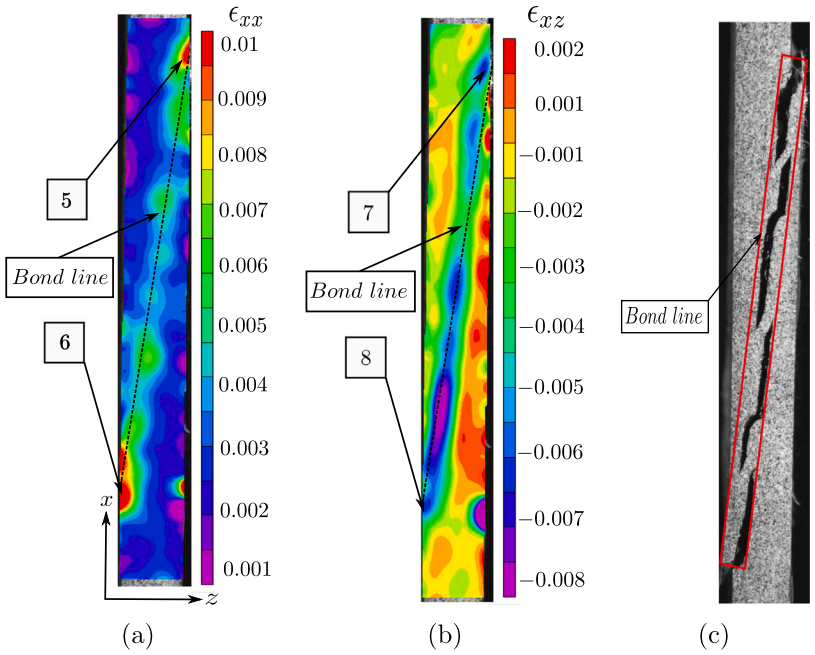

Fig. 10. Strain distributions over the thickness face of the specimen for the single scarf joint quasi-layup obtained from DIC at 6.43 kN load: (a) axial strain, (b) shear strain, and (c) final failure.

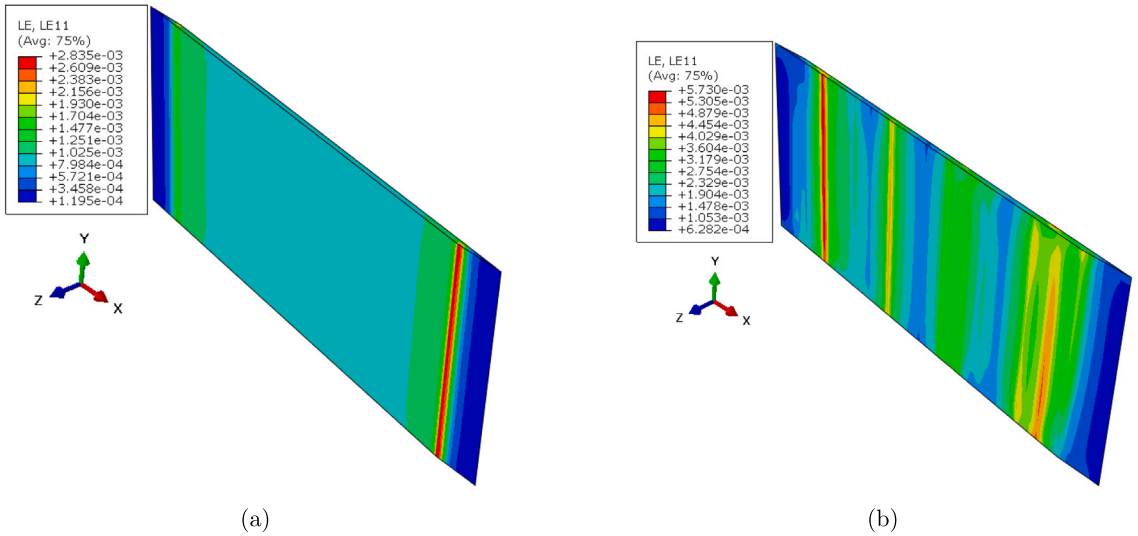

Fig. 11. Axial strain (ϵ_{xx}) contour plots in the adhesive layer of the single scarf joint specimen: (a) UD-layup and (b) quasi-layup.

6.4.2. *Effect of adhesive thickness*

Adhesive thickness is one of the design parameters that influence the strength and stiffness of the joints. The load–displacement curves of the adhesively bonded single scarf joined UD and quasi-isotropic laminates are compared for different values of adhesive thickness as shown in Fig. 24. It is observed that the stiffness decreases with an increase in the thickness of the adhesive. This is due to the reduction of the overlap length for both UD and quasi-isotropic laminates as shown in Fig. 24. The stiffness is greater for the healthy structure as compared to the single scarf bonded UD and quasi-isotropic laminates.

Fig. 25 depicts the normal stress distribution obtained along the normalized bond length of the adhesively bonded single scarf joined UD and quasi-isotropic laminates for different adhesive thicknesses. It is observed that the normal stresses are high at the overlap edges for the thick adhesive case in both UD and quasi-isotropic laminates.

Fig. 26 depicts the peel and shear stress distribution along the adhesive layer obtained in terms of the normalized coordinates for the single scarf quasi-isotropic laminate. It is observed that the peel and shear stress levels are greater for thin adhesive layer configurations.

6.4.3. *Effect of adhesive modulus*

The load–displacement curves of the single scarf joined UD and quasi-isotropic laminates obtained for different values of adhesive modulus are depicted in Fig. 27. It is seen that the joint stiffness increases with adhesive modulus for both UD and quasi-isotropic laminates. The healthy structure is higher stiffness as compared to both the single

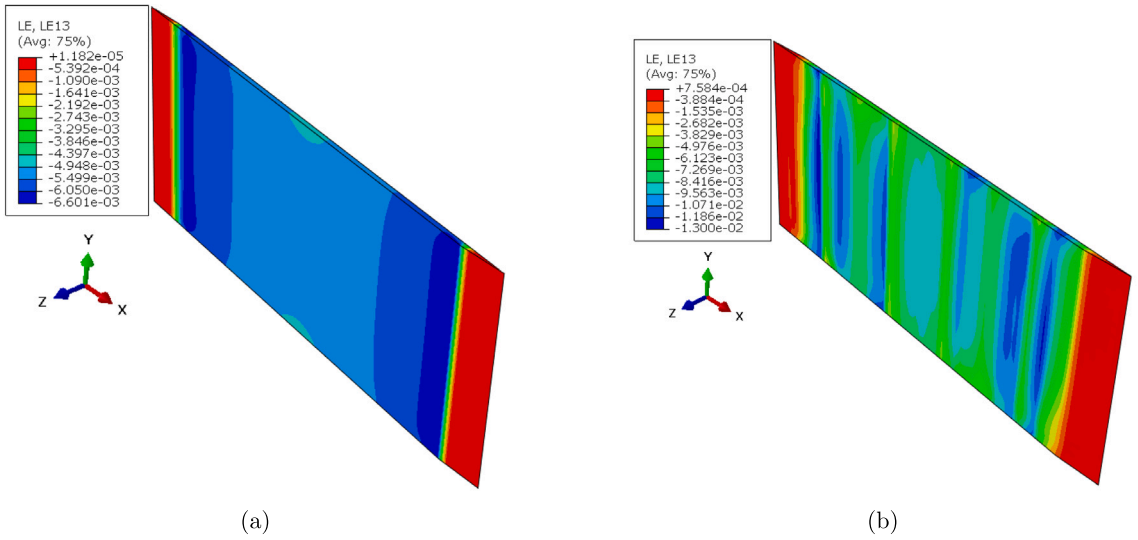

Fig. 12. Shear strain (ϵ_{xz}) contour plots over the adhesive layer of the single scarf joint specimen: (a) UD-layup and (b) quasi-layup.

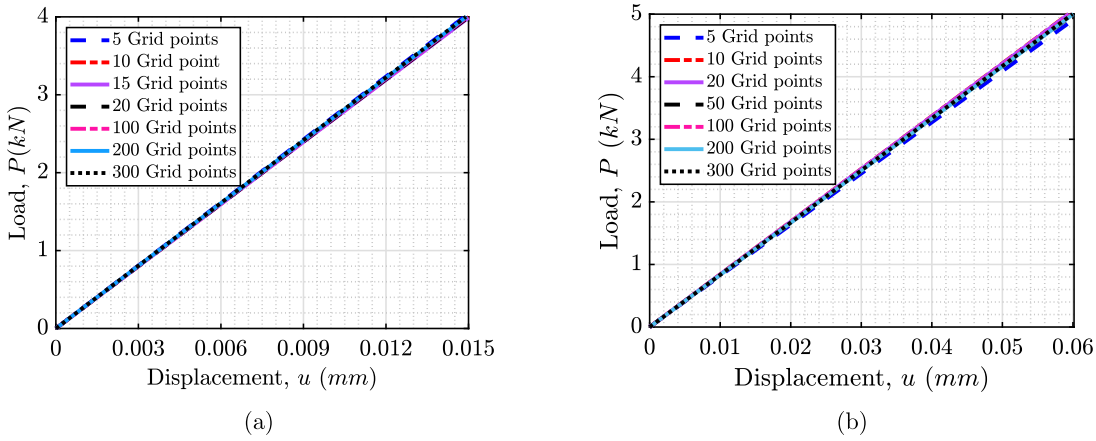

Fig. 13. Convergence study based on the structural level response for the single scarf joint specimen: (a) UD-layup and (b) quasi-layup.

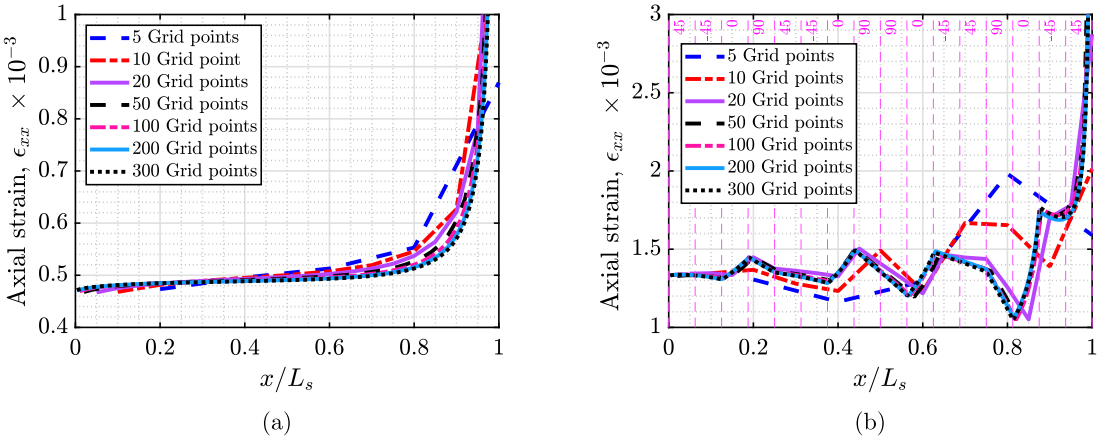

Fig. 14. Convergence study based on the axial strain distribution obtained along the normalized bond length in left adherend of the single scarf joint configuration: (a) UD-layup and (b) quasi-layup.

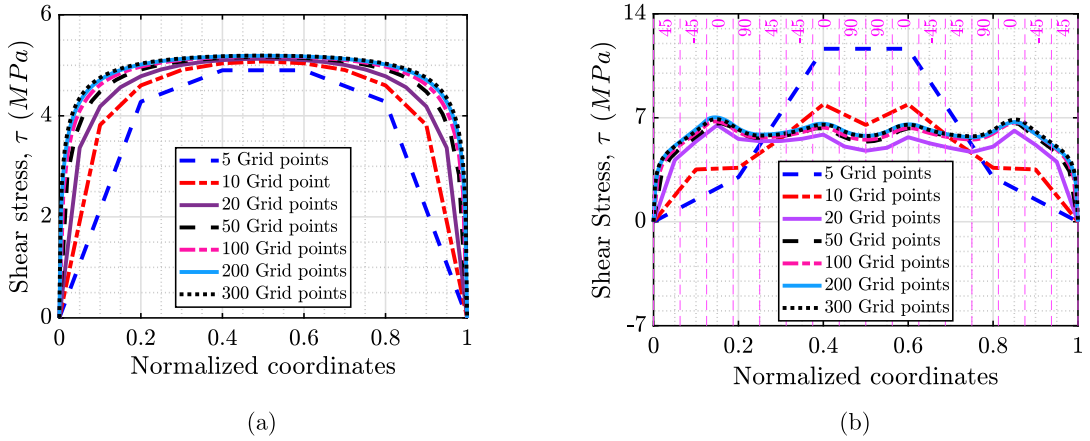

Fig. 15. Convergence study based on the shear stress distribution obtained along the normalized coordinates in the adhesive layer of the single scarf joint configuration: (a) UD-layup and (b) quasi-layup.

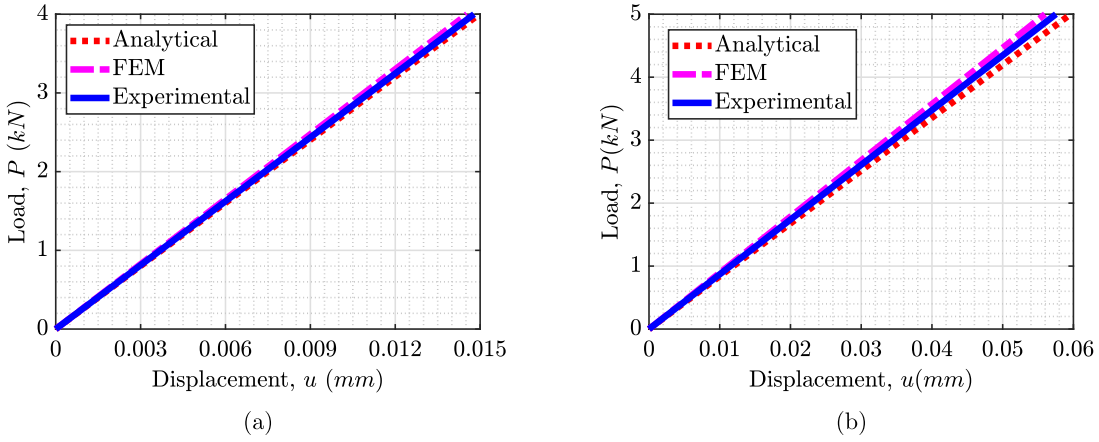

Fig. 16. Load–displacement curves for the single scarf joint configuration: (a) UD-layup and (b) quasi-layup.

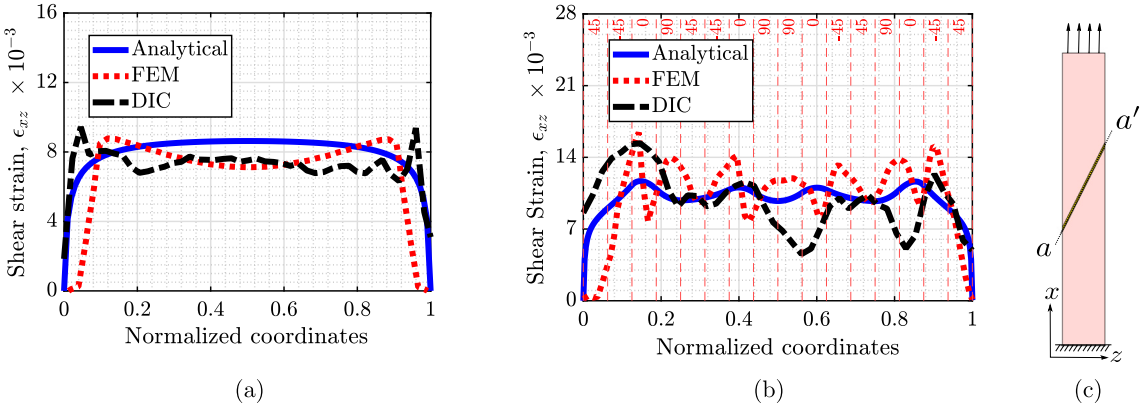

Fig. 17. Shear strain distributions obtained along the normalized coordinates over the adhesive bond in case of a single scarf joint configuration: (a) UD-layup, (b) quasi-layup, and (c) adhesive bondline is depicted by $a - a'$ in the schematic.

scarf joined UD and quasi-isotropic laminates having different adhesive modulus.

Fig. 28 depicts the normal stress distribution obtained along the normalized bond length of the single scarf joined UD and quasi-isotropic laminates predicted for different adhesive moduli. It is observed that the normal stress gets reduced (mildly) with increased adhesive modulus for both UD and quasi-isotropic laminates. Overall, as expected the normal stresses in the adherend are relatively insensitive to changes in the elastic modulus of the adhesive.

This observation is expected as the adherends are the load-carrying member in the joint, while adhesive acts the load transfer element between the adherends. Therefore, any change in the modulus of adhesive does not strongly influence the stress distribution in the adherends.

The peel and shear stress distribution obtained along the normalized coordinates predicted for the different adhesive modulus cases of the adhesively bonded single scarf joined quasi-isotropic laminates are shown in Fig. 29. It is seen that the peel and shear stress magnitude are greater for the higher modulus adhesive case.

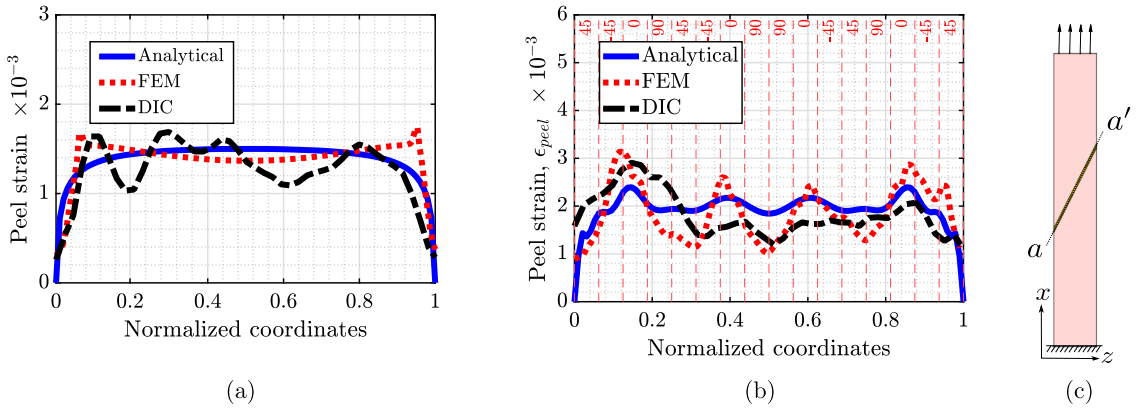

Fig. 18. Peel strain distribution obtained along the normalized coordinates over the adhesive bond in case of a single scarf joint configuration: (a) UD-layup, (b) quasi-layup, and (c) adhesive bondline is depicted by $a - a'$ in the schematic.

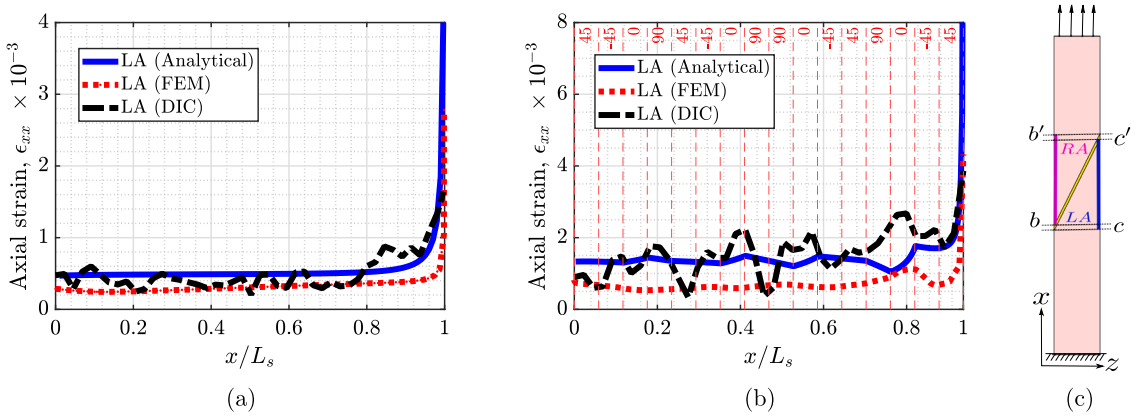

Fig. 19. Axial strain distribution obtained along the normalized bond length over the left adherend (LA) of the single scarf joint configuration: (a) UD-layup, (b) quasi-layup, and (c) location of bond length for the left adherend ($c - c'$).

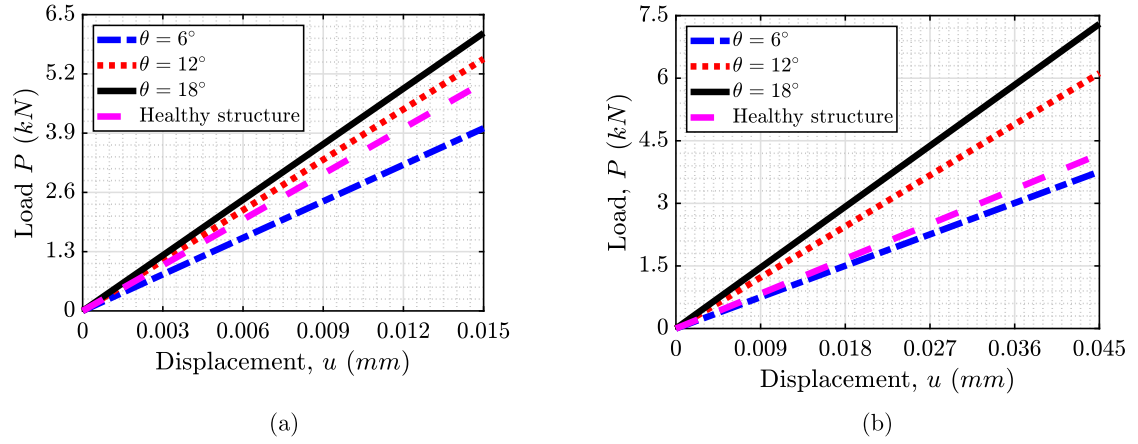

Fig. 20. Load–displacement curves predicted by the analytical model for the single scarf joint configuration: (a) UD-layup and (b) quasi-layup.

From the above results obtained over a parametric study on the effect of adhesive elastic moduli, one could observe that
(i) stiffness of the joint increased
(ii) higher stresses are noted in the adhesive making the joint susceptible to disbond with increasing elastic moduli of adhesive.

Therefore, the choice for the elastic modulus of the adhesive must be appropriately chosen depending on the design needs.

7. Conclusions

In the present work, the mechanical behavior of an adhesively-bonded single scarf joined CFRP UD and quasi-isotropic laminates under tensile loading are studied. The stacking sequence considered in this work is $[0]_{16}$ for the UD-layup and $[45/-45/0/90]_{2s}$ for the quasi-layup. Load–displacement curves are obtained from the analytical

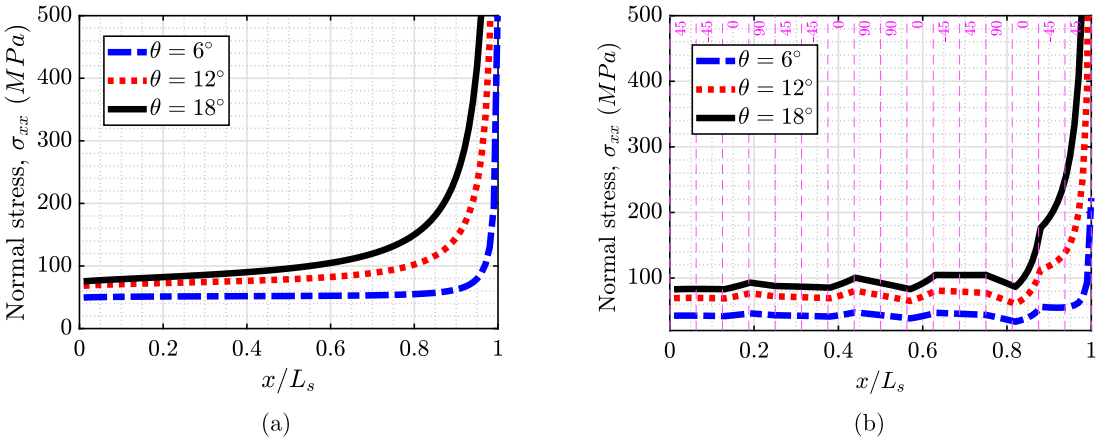

Fig. 21. Normal stress distribution obtained along the normalized bond length over the left adherend of the single scarf joint configuration predicted for different scarf angles: (a) UD-layup and (b) quasi-layup.

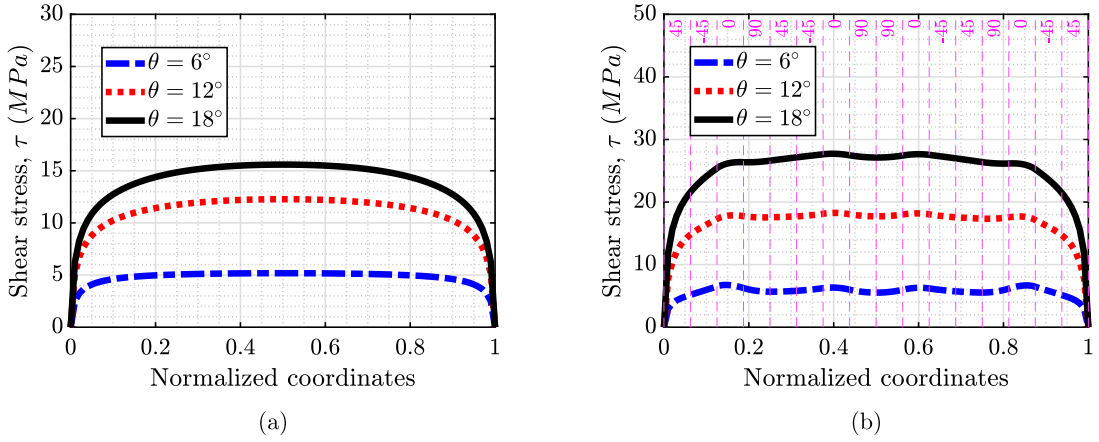

Fig. 22. Shear stress distribution obtained along the normalized coordinates over the adhesive layer in case of single scarf joint configuration predicted for different scarf angles: (a) UD-layup and (b) quasi-layup.

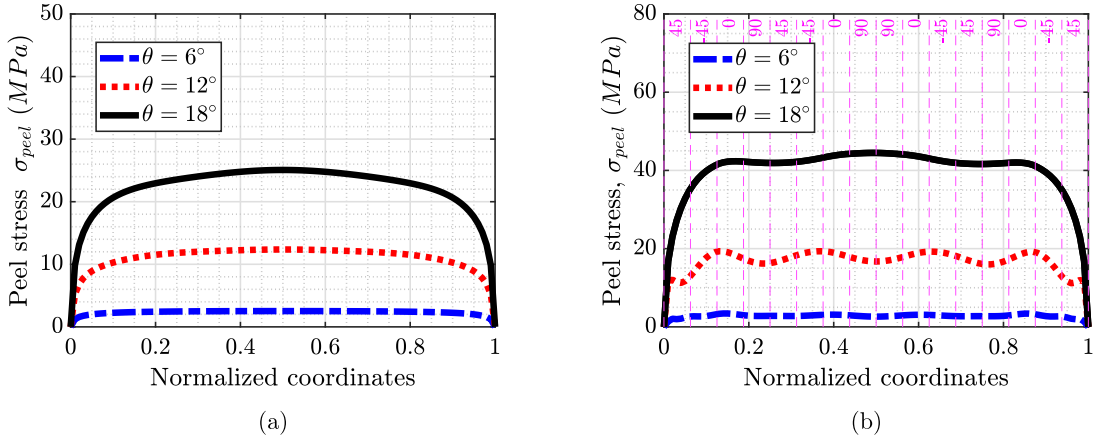

Fig. 23. Peel stress distribution obtained along the adhesive layer in case of single scarf joint configuration predicted for different scarf angles: (a) UD-layup and (b) quasi-layup.

formulation which is then validated with the experimental and FE predictions. The results obtained from the analytical model are in very good agreement with the experimental predictions at a structural level. Further, a detailed parametric study is also carried out involving adhesive thickness, adhesive modulus, and scarf angle on their mechanical behavior. The following are the important take always:

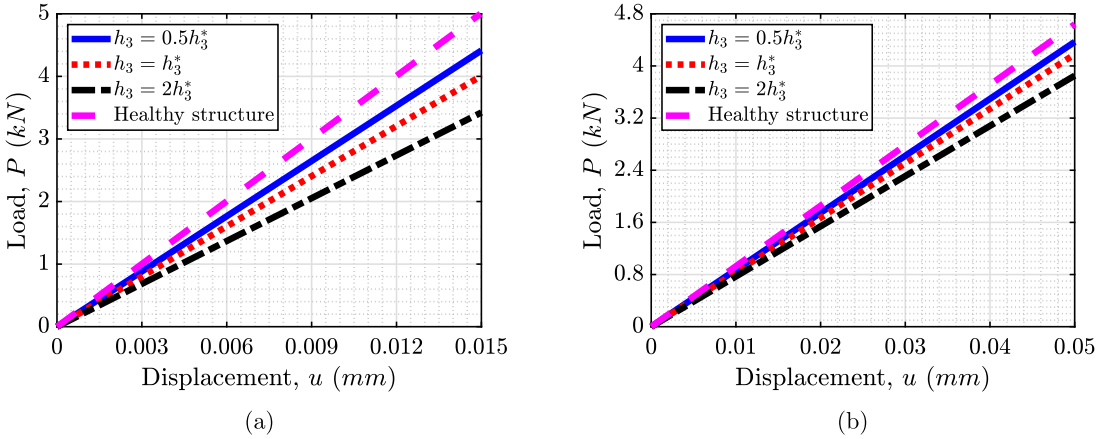

Fig. 24. Load–displacement curves for the single scarf joint specimen predicted for different adhesive thickness: (a) UD-layup (h_3^* = 0.48 mm) and (b) quasi-layup (h_3^* = 0.46 mm).

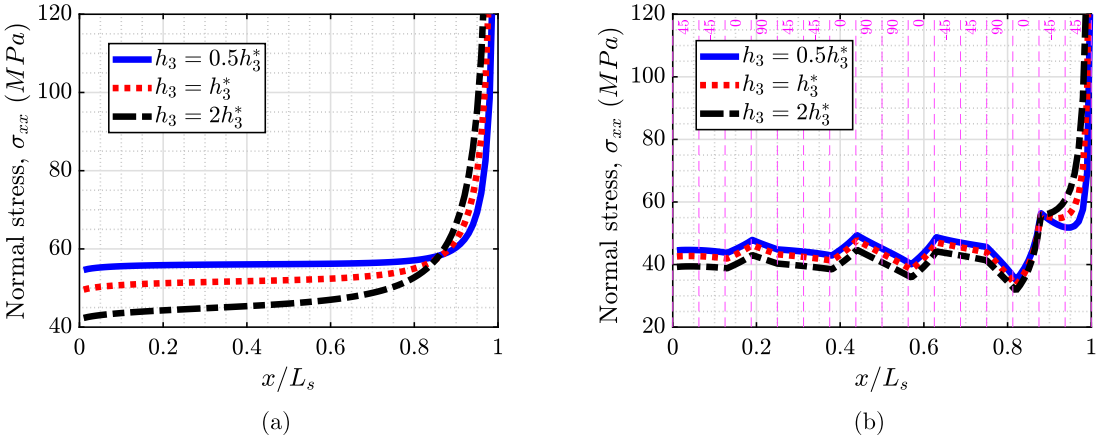

Fig. 25. Normal stress distribution obtained along the normalized bond length over the left adherend of the single scarf joint configuration predicted for different adhesive thickness: (a) UD-layup (h_3^* = 0.48 mm) and (b) quasi-layup (h_3^* = 0.46 mm).

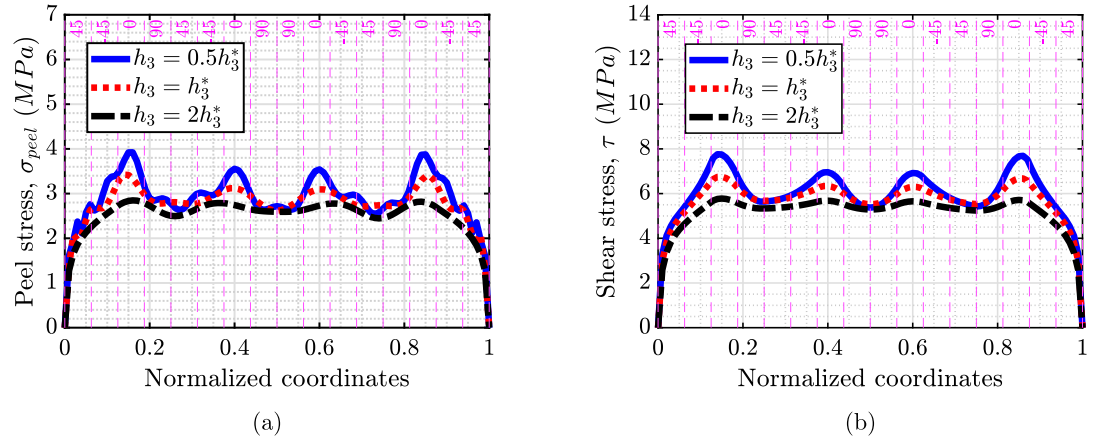

Fig. 26. Stress distribution obtained along the normalized coordinates over the adhesive layer of the single scarf joined quasi-layup configuration predicted for different adhesive thickness (h_3^* = 0.46 mm) (a) peel stress and (b) shear stress.

- From the analytical model, one could observe that the strain concentrations are higher at the overlap edge of the specimen for both single scarf UD and quasi-isotropic laminates. This has been confirmed by the experimental DIC contour plots as well. This points to the overlap edges being a probable location for failure of the adhesive joints.
- Higher magnitude of shear strain is seen in the 0° ply portion, while it is lower in the 90° and 45° plies along the adhesive bond line of the single scarf joint quasi-layup. This points to a possible disbond of the adhesive at 0° ply portion.
- The scarf angle has a strong influence on peel and shear stress magnitude along the bond line, as well as the stiffness of the adhesive joint. It is concluded that an appropriate choice for scarf angle must be made to balance between the stiffness of the adhesive joint and stress concentrations within the adhesive layer at the overlap edges.

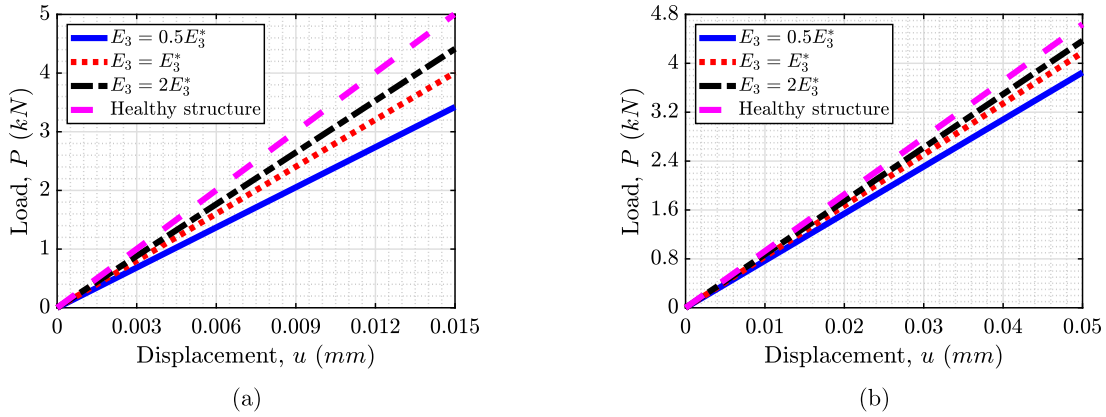

Fig. 27. Load–displacement curves for the single scarf joint specimen predicted for different adhesive modulus (E_3^* = 1.68 GPa): (a) UD-layup and (b) quasi-layup.

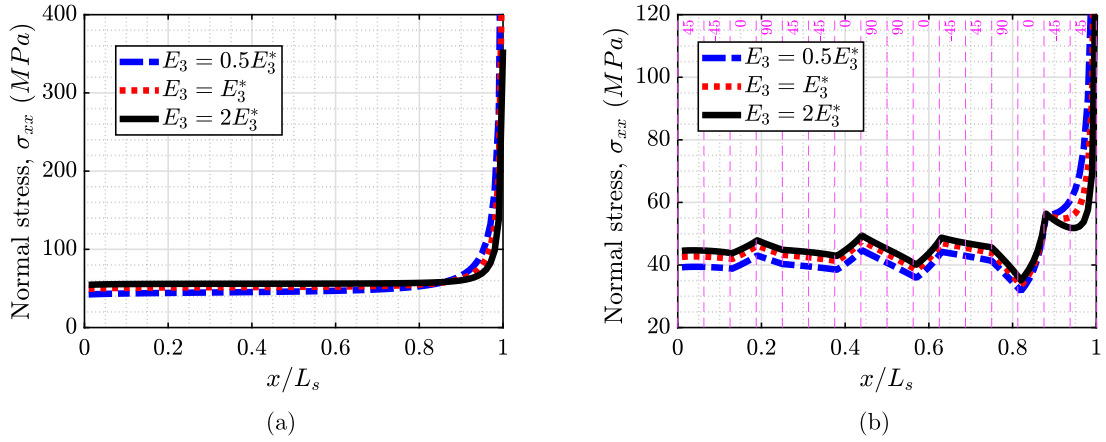

Fig. 28. Normal stress distribution obtained along the normalized bond length in the left adherend of the single scarf joint configuration predicted for different adhesive modulus (E_3^* = 1.68 GPa): (a) UD-layup and (b) quasi-layup.

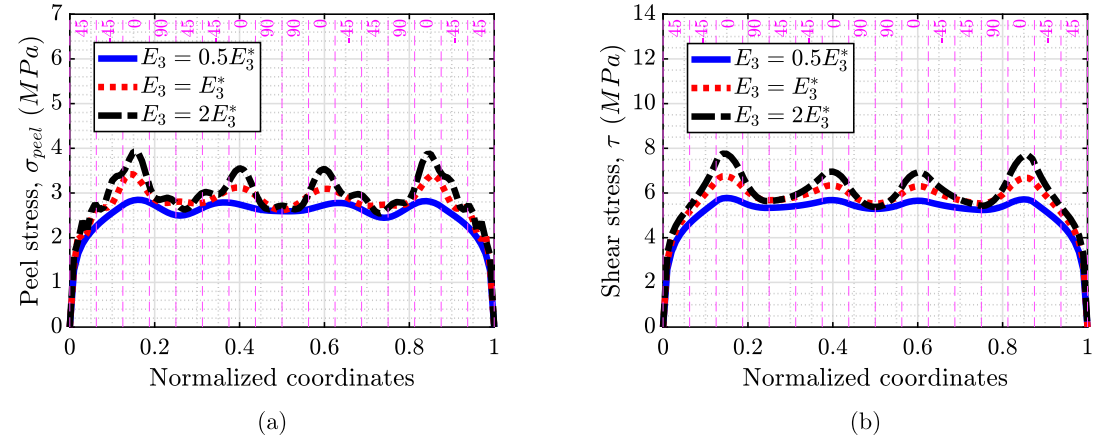

Fig. 29. Peel and shear stress distribution obtained along the normalized coordinates over the adhesive layer of the single scarf joined quasi-layup specimen predicted for different adhesive modulus (E_3^* = 1.68 GPa).

- The joint stiffness decreases with increasing adhesive thickness, while the peel and shear stress magnitude increases with adhesive thickness for the single scarf joined quasi-isotropic laminates. This points to an optimal choice of the thickness for adhesive to balance the stiffness of the adhesive joints with appropriate stresses within the adhesive layer.
- Higher modulus of adhesive provides stiffer joints, but it also introduces higher peel and shear stresses in the case of a single scarf joined quasi-layup specimen.This points to an optimal choice of the modulus of the adhesive to balance the stiffness of the adhesive joints with appropriate stresses within the adhesive layer.

The analytical model developed here is quite accurate and correlates closely with the experimental and FE predictions on the global response. In the later studies, this analytical model will be expanded to predict other joint configurations like a double scarf and stepped-lap joints. Further, the analytical model will be expanded to include nonlinear effects caused via damage accumulation within the adhesively bonded joint.

CRediT authorship contribution statement

Hetram Sonwani: Conceptualization, Methodology, Analysis and interpretation of data, Writing – original draft. **M. Ramji:** Conceptualization, Methodology, Analysis and interpretation of data, Writing – review & editing, Supervision. **Sai Sidhardh:** Conceptualization, Methodology, Analysis and interpretation of data, Writing – review & editing, Supervision.

Declaration of competing interest

The authors declare that they have no known competing financial interests or personal relationships that could have appeared to influence the work reported in this paper.

Data availability

No data was used for the research described in the article.

Acknowledgments

The author also wishes to thank Mr. Raju P., Mr. M. Praveen, Mr. S. Jagadeesan, and all my lab mates for assisting us in conducting the experiments. The authors further thank the staff of the Central Workshop, IIT Hyderabad, Mr. Ajay Kumar, Mr. Promod, Mr. Ajith, Mr. Dhananjay, and Mr. Munugala Dakaiah for helping us with the fabrication of the specimens.

Appendix. Governing equations using equilibrium approach

Previously, in Section 2, one has developed the GDEs for the adhesively bonded single scarf joint following an energy-based approach. In this section, GDEs following the force equilibrium approach is also developed following the approach given in Ref. [49]. Thereby, one can establish the equivalence of these two approaches for modeling the mechanical behavior of adhesively bonded single scarf joints. Note that this derivation is carried out for an isotropic/UD adherend, as done previously in Ref. [38]. The energy approach allows a straightforward extension to quasi-isotropic adherends as seen in § 2.2. In order to derive the governing equations, one must consider the free-body diagram of a representative element. Note that, the domain of the scarf joint is of interest in this study. Therefore, the governing differential equations are derived over this domain alone. More clearly, one can recast the x-axis such that $x = 0$ coincides with the left end of the joint and $x = h/\tan\theta$ is the right end. Although the external loads are applied at the end of the adherends, these loads are transferred to the domain of interest in an appropriate manner.

Fig. A.1 shows an element of the length of $\mathrm{d}x$ comprising the adhesive layer, and both adherends. The free-body diagram of each of the constituents within the element for the left adherend, right adherend, and adhesive are depicted in Fig. A.2.

Resolving forces due to oblique stresses along the $x-z$ direction and then applying the force equilibrium along the x-axis and z-axis gives the following equilibrium equations:

$$\left(\sigma_x + \frac{\mathrm{d}\sigma_x}{\mathrm{d}x}\right)\left(\mathcal{A}_1 + \frac{\mathrm{d}\mathcal{A}_1}{\mathrm{d}x}\right) - \sigma_x\mathcal{A}_1 + (\sigma\sin\theta + \tau\cos\theta)\mathcal{A}_s = 0 \tag{A.1a}$$

$$\left(\tau_{xz} + \frac{d\tau_{xz}}{\mathrm{d}x}\right)\left(\mathcal{A}_1 + \frac{d\mathcal{A}_1}{\mathrm{d}x}\right) - \tau_{xz}\mathcal{A}_1 + (\sigma\cos\theta - \tau\sin\theta)\mathcal{A}_s = 0 \tag{A.1b}$$

$$\left(\sigma'_x + \frac{d\sigma'_x}{\mathrm{d}x}\right)\left(\mathcal{A}_2 + \frac{d\mathcal{A}_1}{\mathrm{d}x}\right) - \sigma'_x\mathcal{A}_2 - (\sigma\sin\theta + \tau\cos\theta)\mathcal{A}_s = 0 \tag{A.1c}$$

$$\left(\tau'_{xz} + \frac{d\tau'_{xz}}{\mathrm{d}x}\right)\left(\mathcal{A}_2 + \frac{d\mathcal{A}_2}{\mathrm{d}x}\right) - \tau'_{xz}\mathcal{A}_2 - (\sigma\cos\theta - \tau\sin\theta)\mathcal{A}_s = 0 \tag{A.1d}$$

In the above equations, σ_x, and σ'_x are the normal stress in the left and right adherends, τ_{xz}, and τ'_{xz} are the shear stress in the left and right adherends, $\mathcal{A}_1$, and $\mathcal{A}_2$ are the cross-sectional areas of the left and right adherends, σ, and τ are the normal and shear stress in the adhesive layer, $\mathcal{A}_s$ is the shear area of the adhesive layer. The expressions for these stresses are identical to those given in Section 2. Note that the unit width of the specimen is considered in this formulation. The GDE obtained for the left adherend along the axial direction can be expressed as:

$$E(h - x\tan\theta)\frac{\mathrm{d}^2u_1}{\mathrm{d}x^2} + (-E\tan\theta)\frac{\mathrm{d}u_1}{\mathrm{d}x} + \left(\frac{E_3}{h_3}\sin\theta\tan\theta + \frac{G_3}{h_3}\cos\theta\right)\Delta u + \left(-\frac{E_3}{h_3}\sin\theta + \frac{G_3}{h_3}\sin\theta\right)\Delta w = 0 \tag{A.2a}$$

Here, E is the elastic modulus and θ is the scarf angle respectively. Similarly, the GDE obtained for the left adherend along the transverse direction can be expressed as:

$$G(h - x\tan\theta)\frac{\mathrm{d}^2w_1}{\mathrm{d}x^2} + (-G\tan\theta)\frac{\mathrm{d}w_1}{\mathrm{d}x} + \left(\frac{E_3}{h_3}\sin\theta - \frac{G_3}{h_3}\sin\theta\right)\Delta u + \left(-\frac{E_3}{h_3}\sin\theta - \frac{G_3}{h_3}\sin\theta\tan\theta\right)\Delta w = 0 \tag{A.2b}$$

In a similar manner, the GDEs for the right adherends along axial and transverse directions can be expressed as:

$$E(x\tan\theta)\frac{\mathrm{d}^2u_2}{\mathrm{d}x^2} + (E\tan\theta)\frac{\mathrm{d}u_2}{\mathrm{d}x} + \left(-\frac{E_3}{h_3}\sin\theta\tan\theta - \frac{G_3}{h_3}\cos\theta\right)\Delta u + \left(\frac{E_3}{h_3}\sin\theta - \frac{G_3}{h_3}\sin\theta\right)\Delta w = 0 \tag{A.2c}$$

$$G(x\tan\theta)\frac{\mathrm{d}^2w_2}{\mathrm{d}x^2} + (G\tan\theta)\frac{\mathrm{d}w_2}{\mathrm{d}x} + \left(-\frac{E_3}{h_3}\sin\theta + \frac{G_3}{h_3}\sin\theta\right)\Delta u + \left(\frac{E_3}{h_3}\cos\theta + \frac{G_3}{h_3}\sin\theta\tan\theta\right)\Delta w = 0 \tag{A.2d}$$

The above equations can be recast as:

$$a_1\frac{\mathrm{d}^2u_1}{\mathrm{d}x} + b_1\frac{\mathrm{d}u_1}{\mathrm{d}x} + c_1\Delta u + d_1\Delta w = 0 \tag{A.3a}$$

$$a_2\frac{\mathrm{d}^2w_1}{\mathrm{d}x} + b_2\frac{\mathrm{d}w_1}{\mathrm{d}x} + c_2\Delta u + d_2\Delta w = 0 \tag{A.3b}$$

$$a_3\frac{\mathrm{d}^2u_2}{\mathrm{d}x} + b_3\frac{\mathrm{d}u_2}{\mathrm{d}x} + c_3\Delta u + d_3\Delta w = 0 \tag{A.3c}$$

$$a_4\frac{\mathrm{d}^2w_2}{\mathrm{d}x} + b_3\frac{\mathrm{d}w_2}{\mathrm{d}x} + c_4\Delta u + d_4\Delta w = 0 \tag{A.3d}$$

where,

$$a_1 = E(h - x\tan\theta), \quad b_1 = -E\tan\theta, \quad c_1 = \left(\frac{E_3}{h_3}\right)\sin\theta\tan\theta + \left(\frac{G_3}{h_3}\right)\cos\theta,$$

$$d_1 = -\left(\frac{E_3}{h_3}\right)\sin\theta + \left(\frac{G_3}{h_3}\right)\sin\theta, \quad a_2 = G(h - x\tan\theta), \quad b_2 = -G\tan\theta,$$

$$c_2 = \left(\frac{E_3}{h_3}\right)\sin\theta - \left(\frac{G_3}{h_3}\right)\sin\theta, \quad d_2 = -\left(\frac{E_3}{h_3}\right)\cos\theta - \left(\frac{G_3}{h_3}\right)\sin\theta\tan\theta,$$

$$a_3 = E(x\tan\theta), \quad b_3 = -b_1, \quad c_3 = -c_1, \quad d_3 = -d_1, \quad a_4 = G(x\tan\theta),$$

$$b_4 = -b_2, \quad c_4 = -\left(\frac{E_3}{h_3}\right)\sin\theta + \left(\frac{G_3}{h_3}\right)\sin\theta, \quad d_4 = -d_2$$

Note that the above equations are coupled linear ordinary differential equations (ODEs) subjected to the following boundary conditions:

$$u_1(0) = 0, \quad w_1(0) = 0, \quad u_2(0) = 0, \quad w_2(0) = 0 \tag{A.4a}$$

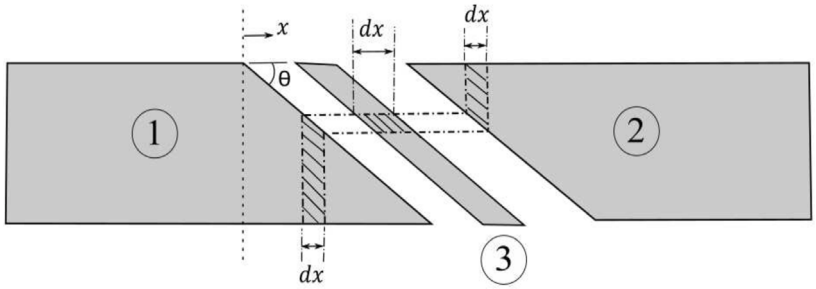

Fig. A.1. Schematic of the element of the single scarf joint which includes adhesive layer, left and right adherends.

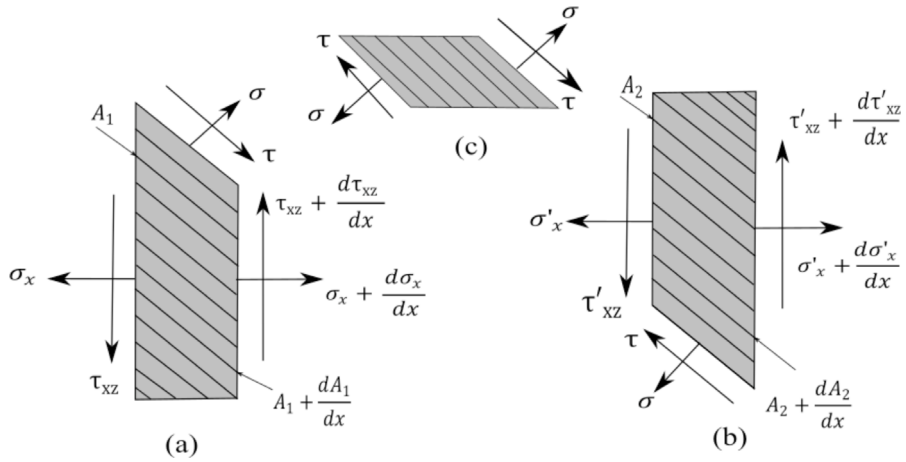

Fig. A.2. Free body diagram of the single scarf joint: (a) left adherend, (b) right adherend, and (c) adhesive layer.

$$u_1(L_s) = u_x, \quad w_1(L_s) = 0, \quad u_2(L_s) = u_x, \quad w_2(L_s) = 0 \tag{A.4b}$$

Note that the above equations correspond to adhesively bonded single scarf joint with UD adherends. These GDEs are identical to those given in Eq. (25) derived for quasi-isotropic adherends considering appropriate material properties.

References

[1] Ozel A, Yazici B, Akpinar S, Aydin MD, Temiz Ş. A study on the strength of adhesively bonded joints with different adherends. Composites B 2014;62:167–74.

[2] Shang X, Marques E, Machado J, Carbas R, Jiang D, Da Silva L. Review on techniques to improve the strength of adhesive joints with composite adherends. Composites B 2019;177:107363.

[3] Bhatia GS, Andrew JJ, Arockiarajan A. Experimental investigation on compressive behaviour of different patch–parent layup configurations for repaired carbon/epoxy composites. J Compos Mater 2019;53(23):3269–79.

[4] Caminero MA, Pavlopoulou S, Lopez-Pedrosa M, Nicolaisson B, Pinna C, Soutis C. Analysis of adhesively bonded repairs in composites: Damage detection and prognosis. Compos Struct 2013;95:500–17.

[5] Tong L, Spelt J, Fernlund G. Strength determination of adhesive bonded joints. In: Recent advances in structural joints and repairs for composite materials. Springer; 2003, p. 27–66.

[6] Katnam KB, Da Silva L, Young T. Bonded repair of composite aircraft structures: A review of scientific challenges and opportunities. Prog Aerosp Sci 2013;61:26–42.

[7] Marques TPZ, Mayer S, Candido GM, Rezende MC. Fractographic analysis of scarf repaired carbon/epoxy laminates submitted to tensile strength. Eng Fail Anal 2021;124:105374.

[8] Bouanani MF, Benyahia F, Albedah A, Aid A, Bouiadjra BB, Belhouari M, et al. Analysis of the adhesive failure in bonded composite repair of aircraft structures using modified damage zone theory. Mater Des 2013;50:433–9.

[9] Vinson JR. Adhesive bonding of polymer composites. Polym Eng Sci 1989;29(19):1325–31.

[10] Mortensen F, Thomsen OT. Analysis of adhesive bonded joints: a unified approach. Compos Sci Technol 2002;62(7–8):1011–31.

[11] Banea MD, da Silva LF. Adhesively bonded joints in composite materials: an overview. Proc Inst Mech Eng L J Mater Des Appl 2009;223(1):1–18.

[12] Budhe S, Banea M, De Barros S, Da Silva L. An updated review of adhesively bonded joints in composite materials. Int J Adhes Adhes 2017;72:30–42.

[13] Neto J, Campilho RD, Da Silva L. Parametric study of adhesive joints with composites. Int J Adhes Adhes 2012;37:96–101.

[14] Ramalho LD, Campilho RD, Belinha J, da Silva LF. Static strength prediction of adhesive joints: A review. Int J Adhes Adhes 2020;96:102451.

[15] Préau M, Hubert P. Processing of co-bonded scarf repairs: void reduction strategies and influence on strength recovery. Composites A 2016;84:236–45.

[16] Shishesaz M, Hosseini M. Effects of joint geometry and material on stress distribution, strength and failure of bonded composite joints: an overview. J Adhes 2018.

[17] Srinivasan D, Padma SR, Idapalapati S. Comparative study of composite scarf and strap joints for equivalent repair signature under uniaxial tension. Composites A 2022;106950.

[18] Cognard J-Y, Leguillon D, Carrere N. Analysis of the influence of geometric parameters on the stress distributions in adhesively bonded scarf joints using 2D models under elastic assumption. J Adhes 2014;90(11):877–98.

[19] He X. A review of finite element analysis of adhesively bonded joints. Int J Adhes Adhes 2011;31(4):248–64.

[20] Bendemra H, Compston P, Crothers PJ. Optimisation study of tapered scarf and stepped-lap joints in composite repair patches. Compos Struct 2015;130:1–8.

[21] Sun L, Tie Y, Hou Y, Lu X, Li C. Prediction of failure behavior of adhesively bonded CFRP scarf joints using a cohesive zone model. Eng Fract Mech 2020;228:106897.

[22] Li J, Yan Y, Zhang T, Liang Z. Experimental study of adhesively bonded CFRP joints subjected to tensile loads. Int J Adhes Adhes 2015;57:95–104.

[23] Cheng P, Gong X-J, Aivazzadeh S, Xiao X. Experimental observation of tensile behavior of patch repaired composites. Polym Test 2014;34:146–54.

[24] Xiaoquan C, Baig Y, Renwei H, Yujian G, Jikui Z. Study of tensile failure mechanisms in scarf repaired CFRP laminates. Int J Adhes Adhes 2013;41:177–85.

[25] Hu F, Soutis C. Strength prediction of patch-repaired CFRP laminates loaded in compression. Compos Sci Technol 2000;60(7):1103–14.

[26] Pinto A, Campilho R, De Moura M, Mendes IR. Numerical evaluation of three-dimensional scarf repairs in carbon-epoxy structures. Int J Adhes Adhes 2010;30(5):329–37.

[27] He D, Sawa T, Iwamoto T, Hirayama Y. Stress analysis and strength evaluation of scarf adhesive joints subjected to static tensile loadings. Int J Adhes Adhes 2010;30(6):387–92.

[28] He D, Sawa T, Karami A. Stress analysis and strength evaluation of scarf adhesive joints with dissimilar adherends subjected to static tensile loadings. J Solid Mech Mater Eng 2009;3(8):1033–44.
[29] Gunnion AJ, Herszberg I. Parametric study of scarf joints in composite structures. Compos Struct 2006;75(1–4):364–76.
[30] Campilho RDSG, De Moura M, Pinto A, Morais J, Domingues J. Modelling the tensile fracture behaviour of CFRP scarf repairs. Composites B 2009;40(2):149–57.
[31] Campilho R, De Moura M, Domingues J. Stress and failure analyses of scarf repaired CFRP laminates using a cohesive damage model. J Adhes Sci Technol 2007;21(9):855–70.
[32] Kumar SB, Sridhar I, Sivashanker S, Osiyemi S, Bag A. Tensile failure of adhesively bonded CFRP composite scarf joints. Mater Sci Eng B 2006;132(1–2):113–20.
[33] Sonat E, Özerinç S. Failure behavior of scarf-bonded woven fabric CFRP laminates. Compos Struct 2021;258:113205.
[34] Wang CH, Gunnion AJ. On the design methodology of scarf repairs to composite laminates. Compos Sci Technol 2008;68(1):35–46.
[35] Wang CH, Gunnion AJ. Optimum shapes of scarf repairs. Composites A 2009;40(9):1407–18.
[36] Baig Y, Cheng X, Hasham HJ, Abbas M, Khan WA. Failure mechanisms of scarf-repaired composite laminates under tensile load. J Braz Soc Mech Sci Eng 2016;38(7):2069–75.
[37] Yoo J-S, Truong V-H, Park M-Y, Choi J-H, Kweon J-H. Parametric study on static and fatigue strength recovery of scarf-patch-repaired composite laminates. Compos Struct 2016;140:417–32.
[38] Matta S, Ramji M. Prediction of mechanical behaviour of adhesively bonded CFRP scarf jointed specimen under tensile loading using localised DIC and CZM. Int J Adhes Adhes 2019;89:88–108.
[39] Alves D, Campilho R, Moreira R, Silva F, Da Silva L. Experimental and numerical analysis of hybrid adhesively-bonded scarf joints. Int J Adhes Adhes 2018;83:87–95.
[40] Khashaba U, Aljinaidi A, Hamed M. Analysis of adhesively bonded CFRE composite scarf joints modified with MWCNTs. Composites A 2015;71:59–71.
[41] Ridha M, Tan V, Tay T. Traction–separation laws for progressive failure of bonded scarf repair of composite panel. Compos Struct 2011;93(4):1239–45.
[42] Hayes-Griss J, Orifici A, Khatibi AA. An improved progressive failure modelling and damage tolerant design methodology for composite scarf joints with bondline flaws. Composites A 2020;131:105776.
[43] Adin H. The investigation of the effect of angle on the failure load and strength of scarf lap joints. Int J Mech Sci 2012;61(1):24–31.
[44] Hayes-Griss J, Gunnion A, Khatibi AA. Damage tolerance investigation of high-performance scarf joints with bondline flaws under various environmental, geometrical and support conditions. Composites A 2016;84:246–55.
[45] Gacoin A, Lestriez P, Assih J, Objois A, Delmas Y. Comparison between experimental and numerical study of the adhesively bonded scarf joint and double scarf joint: Influence of internal singularity created by geometry of the double scarf joint on the damage evolution. Int J Adhes Adhes 2009;29(5):572–9.
[46] Breitzman TD, Iarve EV, Cook B, Schoeppner G, Lipton R. Optimization of a composite scarf repair patch under tensile loading. Composites A 2009;40(12):1921–30.
[47] Hart-Smith L. Adhesive-bonded scarf and stepped-lap joints. 1973.
[48] Helms JE, Yang C, Pang SS. Strain distribution in a taper-taper adhesive-bonded joint in a composite flat plate. J Thermoplast Compos Mater 1996;9(3):280–91.
[49] Helms Jr JE. Analysis of taper-taper adhesive-bonded joints in composite plates under tension and cylindrical bending. Louisiana State University and Agricultural & Mechanical College; 1998.
[50] Wang S, Xie Z, Li X. On adhesively bonded stepped-scarf joint: an analytical model and its validation. Mech Adv Mater Struct 2021;28(9):938–51.
[51] Erdogan F, Ratwani M. Stress distribution in bonded joints. J Compos Mater 1971;5(3):378–93.
[52] Liu B, Xu F, Feng W, Yan R, Xie W. Experiment and design methods of composite scarf repair for primary-load bearing structures. Composites A 2016;88:27–38.
[53] Gleich D, Van Tooren M, De Haan P. Shear and peel stress analysis of an adhesively bonded scarf joint. J Adhes Sci Technol 2000;14(6):879–93.
[54] Jones RM. Mechanics of composite materials. CRC Press; 2018.